

Chandra survey in the AKARI North Ecliptic Pole Deep Field. I. X-ray data, point-like source catalog, sensitivity maps, and number counts

M. Krumpe,^{1,3*} T. Miyaji,^{2,3} H. Brunner,⁴ H. Hanami,⁵ T. Ishigaki,⁵ T. Takagi,⁶ A. G. Markowitz,^{3,7} T. Goto,⁸ M. A. Malkan,⁹ H. Matsuhara,^{6,10} C. Pearson,^{11,12,13} Y. Ueda,¹⁴ and T. Wada⁶

¹European Southern Observatory, ESO Headquarters, Karl-Schwarzschild-Straße 2, 85748 Garching bei München, Germany

²Instituto de Astronomía, Universidad Nacional Autónoma de México, Carret. Tijuana-Ensenada, Ensenada 22860, BC, Mexico (mailing addr. P.O. Box 439027, San Diego, CA, 92143, USA)

³University of California, San Diego, Center for Astrophysics and Space Sciences, 9500 Gilman Dr., La Jolla, CA, 92093-0424, USA

⁴Max-Planck-Institut für extraterrestrische Physik, Gießenbachstraße, 85748 Garching bei München, Germany

⁵Iwate University, 3-18-8 Ueda, Morioka, Iwate, 020-8550, Japan

⁶Institute of Space and Astronautical Science, Japan Aerospace Exploration Agency, Sagami-hara, 229-8510, Kanagawa, Japan

⁷Karl Remeis Observatory and Erlangen Centre for Astroparticle Physics, Sternwartstraße 7, 96049 Bamberg, Germany; Alexander von Humboldt Fellow

⁸Institute for Astronomy, University of Hawaii 2680 Woodlawn Drive, Honolulu, HI, 96822, USA

⁹University of California, Los Angeles, Division of Astronomy & Astrophysics, 430 Portola Plaza, Los Angeles, CA, 90095-1547, USA

¹⁰Department of Space and Astronautical Science, The Graduate University for Advanced Studies, Shonan Village, Hayama, Kanagawa, 240-0193, Japan

¹¹RAL Space, STFC Rutherford Appleton Laboratory, Didcot, Oxon, OX11 0QX, UK

¹²The Open University, Milton Keynes, MK7 6AA, UK

¹³University of Oxford, Keble Rd, Oxford, OX1 3RH, UK

¹⁴Department of Astronomy, Kyoto University, Kyoto, 606-8502, Japan

Released 2014 January 17

ABSTRACT

We present data products from the 300 ks *Chandra* survey in the AKARI North Ecliptic Pole (NEP) deep field. This field has a unique set of 9-band infrared photometry covering 2–24 μm from the AKARI Infrared Camera, including mid-infrared (MIR) bands not covered by *Spitzer*. The survey is one of the deepest ever achieved at $\sim 15 \mu\text{m}$, and is by far the widest among those with similar depths in the MIR. This makes this field unique for the MIR-selection of AGN at $z \sim 1$.

We design a source detection procedure, which performs joint Maximum Likelihood PSF fits on all of our 15 mosaicked *Chandra* pointings covering an area of 0.34 deg^2 . The procedure has been highly optimized and tested by simulations. We provide a point source catalog with photometry and Bayesian-based 90 per cent confidence upper limits in the 0.5–7, 0.5–2, 2–7, 2–4, and 4–7 keV bands. The catalog contains 457 X-ray sources and the spurious fraction is estimated to be ~ 1.7 per cent. Sensitivity and 90 per cent confidence upper flux limits maps in all bands are provided as well.

We search for optical MIR counterparts in the central 0.25 deg^2 , where deep Subaru Suprime-Cam multiband images exist. Among the 377 X-ray sources detected there, ~ 80 per cent have optical counterparts and ~ 60 per cent also have AKARI mid-IR counterparts. We cross-match our X-ray sources with MIR-selected AGN from Hanami et al. Around 30 per cent of all AGN that have MID-IR SEDs purely explainable by AGN activity are strong Compton-thick AGN candidates.

Key words: methods: data analysis – surveys – galaxies: active – X-ray: galaxies.

1 INTRODUCTION

The search for Compton-thick absorbed (CT) AGN and the quantification of their contribution to the total accretion

* E-mail: mkrumpe@ucsd.edu

onto supermassive black holes (SMBHs) across cosmological time are still fundamental questions of considerable interest in X-ray astronomy. These CT AGN escape direct detection by imaging surveys in X-rays with *XMM-Newton* and *Chandra*, as these instruments are only sensitive to radiation below ~ 10 keV.

Compton-thick absorbed AGN are required by population synthesis models of the Cosmic X-ray Background (CXB; e.g., Ueda et al. 2003; Gilli et al. 2007) to reproduce its 30 keV peak, although the amount of contribution from such sources is highly model-dependent. Direct detections of the AGN in this population and quantifying their contribution to the SMBH accretion is also of utmost importance for quantifying ‘‘Soltan’s (1982) argument’’ on the comparison of historical accretion (traced by the AGN activity) with the present-day mass density of SMBHs.

Mid infra-red (MIR) emission is another excellent probe of the energy output from AGN including the CT AGN. Unlike X-rays, the MIR emission of extragalactic objects is relatively unaffected by absorption from dust/gas and is almost isotropic. In the presence of an AGN, dust particles are heated to temperatures higher than those associated with star formation activity. Therefore, AGN activity can be identified by investigating the IR spectral energy distribution (SED). The emission from the AGN-heated dust fills the ‘‘valley’’ between the stellar photospheric emission and the warm dust associated with star formation, producing a power-law like continuum over the rest frame 3–8 μm bands. With the advent of the *Spitzer Space Telescope*, IR color diagnostics and SEDs have been used to search for CT AGN by selecting IR AGN candidates (e.g., Martínez-Sansigre et al. 2005; Brand et al. 2006; Lacy et al. 2007; Donley et al. 2012). Mid-IR selection techniques based on *AKARI* data have also been used to identify large AGN samples (e.g., Toba et al. 2014).

AKARI was a Japanese IR astronomical satellite (Matsuhara et al. 2005; Murakami et al. 2007) launched in February 2006 with a 68.5 cm telescope, which concluded its operation in November 2011. In addition to the well-known mid- to far-IR all-sky surveys (Ishihara et al. 2010), *AKARI* also performed spectroscopic surveys, deep imaging surveys in 13 bands ranging from 2–160 μm , as well as pointed observations. The IR Camera (IRC) on *AKARI* provided near-IR (NIR) to mid-IR (MIR) measurements with continuous wavelength coverage over 2–25 μm in 9 filters. This fills the 9–20 μm gap between the *Spitzer* IRAC+MIPS instruments (see figure 2 in Matsuhara et al. 2006) and allows efficient selection of AGN at $0.5 \lesssim z \lesssim 1.5$ in the IR. Due to orbital constraints, deep and large pointing surveys were only possible close to the ecliptic poles. As a legacy programme of *AKARI*, around 13 per cent of all pointed observation during its liquid helium phase were performed in the North Ecliptic Pole (NEP). The survey had a sensitivity limit of $\leq 117 \mu\text{Jy}$ at 15 μm (5σ) over the full area of 0.4 deg^2 , and reached $\leq 60 \mu\text{Jy}$ at 15 μm in 30 per cent of the area (Wada et al. 2008). The *AKARI* NEP deep field is one of the deepest surveys at $\sim 15 \mu\text{m}$, and is by far the widest among those with similar depths. Its area is five times larger than the *Spitzer* IRS 16 μm ‘peak up’ imaging survey (Teplitz et al. 2005). With the unique deep imaging coverage of the 11–19 μm regime with three filters, the *AKARI* NEP deep field com-

plements larger programs such as the COSMOS, GOODS, and Extended Groth Strip (EGS) surveys.

Extensive multi-wavelength follow-up data cover the *AKARI* NEP deep field. This includes the full available wavelength range from radio, sub-millimeter (*Herschel*), far-infrared, near-infrared, optical, through the UV. The *Chandra* observation, presented in this paper, therefore extends even further the baseline of the wavelength coverage in this field. In addition to the deep near-infrared and optical multi-color images which are used to provide accurate photometric redshifts, star-formation rates, stellar masses, etc., a large number of optical spectra (~ 1000) for selected objects have already been obtained using Subaru/FOCAS, Subaru FMOS, Keck DEIMOS, GTC OSIRIS (long-slit), MMT Hectospec, and the 3.5 m WIYN telescope. A catalog from the latter two instruments has been published by Shim et al. (2013). Further spectroscopic follow-up programs are currently being prepared, including a scheduled GTC/OSIRIS (MOS) program.

In view of these, we have initiated a *Chandra* survey of the field. We have achieved a total exposure of 300 ks over fifteen ACIS-I observations, which include our own program and archival data. In this paper, we explain our improved source detection procedure on a highly-overlapping mosaic of ACIS data and publish our source list. In addition, we explain our sensitivity map and Bayesian-based upper limit determination, and present the $\log N - \log S$ relation. A quick-look comparison with MIR-selected AGN is also presented. More detailed analysis and interpretations of the Compton-thick populations implied by these observations will be presented in a future paper (Miyaji et al., in preparation).

This paper is organized as follows. In Sect. 2, we describe the *Chandra* observation in the *AKARI* NEP deep field, while Sect. 3 details the data reduction. The generation of simulated data and how these data are used to explore the best-suited source detection algorithm is illustrated in Sect. 4. Section 5 gives details on the properties of the (real data) source catalog and the generation of the sensitivity maps, and characterizes the survey. Our results are discussed in Sect. 6, and we summarize our work in Sect. 7. Throughout the paper, we use a cosmology of $\Omega_M = 0.3$, $\Omega_\Lambda = 0.7$, and $h = 70 \text{ km s}^{-1} \text{ Mpc}^{-1}$, consistent with *WMAP* data release 7 (Larson et al. 2011; Table 3). We use AB magnitudes throughout the paper. All uncertainties represent a 1σ (68.3 per cent) confidence interval unless otherwise stated.

2 OBSERVATIONS

The *AKARI* NEP deep field was observed with *Chandra* between December 2010 and April 2011 (cycle 12). Twelve individual ACIS-I pointings with a total exposure time of 250 ks were planned (Table 1). The central position of the mosaicked observation is roughly R.A. = 17h 55m 24s and decl. = $+66^\circ 33' 33''$. We use the ACIS CCDs I0-I3 in timed exposure (TE) mode. To exploit the maximum amount of information possible, the very faint (VF) telemetry format is applied.

During one of the observations (OBSID 12934), one of the four CCDs (I0) did not work properly. This field was therefore later reobserved as OBSID 13244. We use all data,

Table 1. Summary of the individual *Chandra* pointings in the *AKARI* NEP Deep Field.

OBSID	R.A. [deg]	decl. [deg]	Roll [deg]	Exp. time [ks]	Date [Mon-dd-yyyy]	#sources (<i>ML</i> > 10)	#offset (<i>ML</i> > 10)	Δx [arcsec]	Δy [arcsec]
12925	268.543481	66.766075	104.2	23.75	Apr-02-2011	54	23	-0.09	+0.08
12926	268.545420	66.658132	98.2	17.83	Apr-01-2011	46	20	-0.15	+0.58
12927	268.551589	66.550512	80.1	23.34	Mar-09-2011	58	20	+0.01	+0.88
12928	268.571772	66.446479	12.2	35.59	Jan-01-2011	83	32	+0.03	+0.15
12929	268.845432	66.800429	85.7	11.90	Mar-16-2011	40	21	+0.16	+0.60
12930	268.851257	66.652304	98.2	14.57	Apr-01-2011	52	24	-0.03	+0.30
12931	268.880422	66.622862	85.7	13.58	Mar-16-2011	49	23	-0.06	+0.63
12932	268.845505	66.450367	85.7	13.88	Mar-18-2011	46	20	+0.08	+0.33
12933	269.164430	66.795924	7.8	23.75	Dec-28-2010	68	34	-0.07	+0.14
12934 ^a	269.143141	66.683887	80.1	14.86	Mar-07-2011	38	19	-0.09	+0.17
12935	269.141210	66.567043	85.7	16.84	Mar-15-2011	55	25	-0.08	+0.61
12936	269.162197	66.447242	18.1	34.61	Jan-08-2011	84	32	-0.07	+0.23
13244	269.136959	66.683144	98.2	14.86	Apr-02-2011	49	30	-0.17	+0.21
10443 ^b	269.331497	66.489757	272.2	21.75	Sep-21-2009	58	27	+0.06	+0.99
11999 ^b	269.331414	66.489748	272.2	24.70	Sep-26-2009	73	33	0.00	+0.93
Total	268.850000	66.559167	—	302.81	—	—	—	—	—

^a ACIS CCD I0 did not work during this observation. The observation was repeated as 13244. ^b Archival observation from cycle 10.

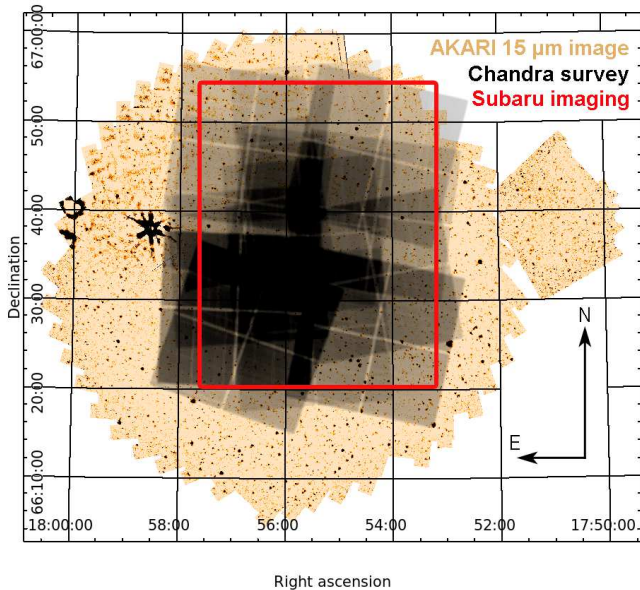


Figure 1. Set-up of the ACIS-I pointing pattern in the *AKARI* NEP deep field. The yellow background image is the $15\ \mu\text{m}$ *AKARI* image. The red box shows the position of the deep Subaru/Suprime-Cam imaging data, while the black filled area illustrate the positions and the summed depths of the individual *Chandra* pointings.

including OBSID 12934, for the data reduction described in Sect. 3.

In addition we include two *Chandra* ACIS-I pointings from the archive, which have observed the southeast corner of the *AKARI* NEP deep field (sequence number 800804, PI: Lubin, cycle 10). The goal of the original proposers of these two observations was to map the AGN population in the X-ray cluster RXJ1757.3+6631 (Rumbaugh et al. 2012). In our analysis, we correctly account for their chosen CCD aim-point offset of 6 mm in the z-direction, which corresponds to 123 arcsec.

The total area covered by our *Chandra* mosaicked sur-

vey is $\sim 0.34\ \text{deg}^2$. Deep optical and near-infrared imaging of a subregion covering $26.3\ \text{arcmin} \times 33.7\ \text{arcmin}$ ($\sim 0.25\ \text{deg}^2$) has been obtained with Subaru/Suprime-Cam. Since the additional *Chandra* ACIS-I pointings overlap almost entirely with pointing 12936, the whole survey can be best described by a dense tiling of a 3×4 ACIS-I pointing pattern. This layout utilizes the sharp *Chandra* PSF over the whole Subaru field to provide unambiguous identification (Figure 1). The observation has been designed to reach an approximately homogeneous coverage of typically $\sim 30\text{--}40$ ks if only off-axis angles with less than 7 arcmin in the individual pointings are considered. Therefore, the spacing between the pointings is ~ 7 arcmin in right ascension and declination. The observation in the northwestern corner of the grid was slightly shifted towards the central position of the field, since the outer region of this pointing is not covered by the *AKARI* $15\ \mu\text{m}$ image. In the region with the additional pointings from the archive (OBSIDs 10443 and 11999), we reach a depth of ~ 80 ks.

3 DATA REDUCTION

We downloaded the pipeline products from the latest available reprocessing run of *Chandra* data (Series IV¹, February 2012). The data reduction pipeline includes cleaning of bad pixels, cosmic ray rejection, etc. The new reprocessing implements some improvement to previous versions that are also important for our scientific goals. For example, it applies improved algorithms for ACIS cosmic-ray afterglow removal, bright bias events, and ACIS time dependent gain. We use the unbinned data. Consequently, one ACIS-I CCD pixel corresponds to 0.492 arcsec.

¹ <http://cxc.cfa.harvard.edu/cda/repro4.html>

3.1 Chandra data reduction with CIAO

We use the standard CIAO 4.4 software tools (Fruscione et al. 2006) for the further data processing and reduction. First, we check for flaring events in the individual observations where the count rate in the 0.5–7 keV band is 4σ above the variance of the mean count rate. Based on the light curves in 200 s bins, only OBSID 12927 is affected by a very short ~ 0.5 ks flare event, which we removed from the observation. We created images and event lists for five different energy bands: 0.5–2, 2–4, 4–7, 0.5–7, and 2–7 keV. A color-coded (by photon energy) image of the *Chandra*/*AKARI* NEP deep field in the first three bands is shown in Figure 2.

As the aimpoints in OBSIDs 10443 and 11999 are significantly shifted, the outer area of the images have an off-axis angle of more than 12 arcmin. However, the *Chandra* PSF library contains data only up to an off-axis angle 12 arcmin. In all data reduction steps we therefore exclude areas outside this limit in OBSIDs 10443 and 11999.

To merge all individual observations into a single observation, the CIAO tool `reproject_events` is used to compute new sky coordinates for the individual event files of the observations. The world coordinate system (WCS) of the central observation 12931 is chosen as the common standard of reference. Then we compute instrument maps (effective area as a function of detector position), transform the image coordinates to the corresponding sky coordinates, and generate exposure maps for all observations. These procedures correspond to the CIAO tasks `mkinstmap`, `get_sky_limits`, and `mkexpmap`. Due to the strong energy dependence of the effective area, we compute weighted instrument maps by using a weighted spectrum file with a photon index of $\Gamma = 1.4$ and an absorbing column $N_{\text{H,Gal}} = 4.0 \times 10^{20} \text{ cm}^{-2}$ (Galactic H I Leiden/Argentine/Bonn survey map by Kalberla et al. 2005) for the central position of the *Chandra*/*AKARI* NEP deep field.

4 SIMULATED DATA AND OPTIMIZED POINT SOURCE DETECTION

An optimal point source detection algorithm needs to account for the observed source counts, background level, and point spread function (PSF) at the focal plane position of each source. In the case of mosaicked observations, such as the *Chandra*/*AKARI* NEP deep survey, most sources are observed multiple times in overlapping pointings with different background levels and at different focal plane positions, corresponding to different PSF shapes and sizes. To maximize the detection sensitivity, and to extract optimal source parameters, such observations need to be processed simultaneously (jointly), considering the appropriate PSF and background level at the position of each source in each pointing. This is of particular importance in the case of *Chandra*, where the half energy width of the on-axis and off-axis PSF differs by more than a factor of 10.

To fine-tune and test the source detection algorithm, we generate five simulated data sets of the *Chandra*/*AKARI* NEP deep field with exactly the same set-up as the real data (Table 1). The advantage of simulated data is that we know the exact position and counts of each individual input

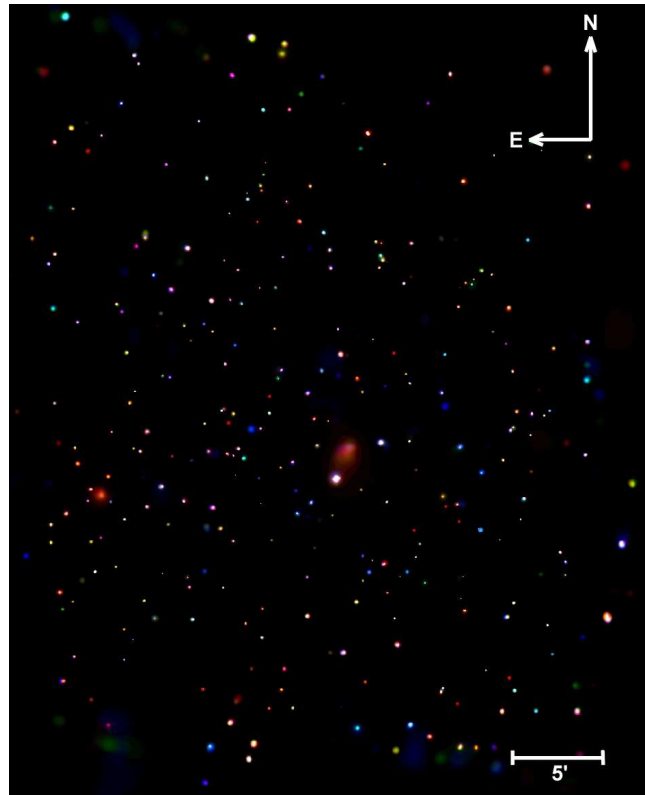


Figure 2. X-ray color-coded image of the *Chandra*/*AKARI* NEP deep field. The colors correspond to the photon energy bands of 0.5–2 keV (red), 2–4 keV (green), and 4–7 keV (blue). In order to display the point sources clearly we applied an adaptive smoothing filter to the individual images using the CIAO tool `csmooth`. We also show a 5 arcmin scale and the orientation of the image.

source. Therefore, we can directly compare the output of the potential source detection software to the input catalog, make comparisons, and draw conclusions about potential improvements to the algorithm. The goals are to determine the best-suited source detection work sequence for our specific data set, and to test new improvements in the code. The final source detection algorithm is chosen to minimize the number of spurious detection (reliability), maximize the number of detection of input sources (completeness), and recover the positions and counts of the input sources as well as possible (accuracy).

4.1 Creating the simulated data

The simulated *Chandra* data of the *AKARI* NEP deep field have been generated using the following strategy. A hypothetical source list that has the same statistical properties, e.g., flux distribution and angular structure, has to be generated. This source list should contain sources fainter than the detection limit of our *Chandra* observations, so that the structure of the unresolved background can be simulated. For this purpose, we use the sources from the 4 Ms *Chandra* deep field South (CDF-S) Xue et al. (2011).

Since the solid angle of the most sensitive part of the CDF-S is much smaller than our *AKARI* NEP deep field field of view, we mosaic the template CDF-S source list to fill the area of our field. We take the following procedure

in generating simulated event lists corresponding to each of our individual OBSIDs.

(i) We select those CDF-S sources from Xue et al. (2011) with a 0.5–8 keV flux of $S_x > 1 \times 10^{-16} \text{ erg s}^{-1} \text{ cm}^{-2}$. This is much fainter than the faintest detectable source in our dataset, and thus we simulate sources that would be detected as well as those that would partially contribute to unresolved background.

(ii) The entire AKARI NEP field is divided into 3×4 sections without overlaps. The sections are arranged in a grid of $\Delta \text{R.A.} = 0.2^\circ / \cos(\text{decl.}_c)$, where decl._c is the declination of the section center, and $\Delta \text{decl.} = 0.175^\circ$.

(iii) The CDF-S sources are mapped into each of the 3×4 sections, such that the CDF-S center is mapped into the center of the individual section, the linear scale is unchanged, and rotation around the center is randomized. If the mapped position is outside of the section, we do not include it in the input source list.

(iv) For each mapped source, we assign the 0.5–8 keV photon fluxes and the effective photon index given by Xue et al. (2011). In order to avoid duplicating the same flux 12 times in the input source list, we assigned a 0.5–8 keV flux that randomly deviates from the original flux of the CDF-S source. For sources with 0.5–8 keV flux $S_x > 1 \times 10^{-14} \text{ erg s}^{-1} \text{ cm}^{-2}$, we randomly assigned a flux that is between 1/3 and 3 times the original flux, in such a way that the probability distribution follows the Euclidean $N(> S) \propto S^{-1.5}$ relation. For fainter sources, we assigned a flux that is between 1/1.5 and 1.5 times the original, following the cumulative probability distribution of $N(> S) \propto S^{-1}$.

(v) We generate simulated event lists for the input sources (with assigned 0.5–8 keV fluxes and effective photon indices) for each of our Chandra OBS-IDs in the AKARI NEP deep field, using the actual aspect solutions and exposure times of the observation. This simulation uses Marx² version 5.0.0. Since we use a common input source list for simulating each Chandra OBSID, it simulates correctly the properties of overlapped data sets.

(vi) We add background events to the simulated Marx source event lists. The background events are derived from the real data background images produced during the source detection in three bands (0.5–2, 2–4, and 4–7 keV), with an emldetect maximum likelihood threshold $ML = 9.5$ and a source cutout radius of 20 arcsec. Changing the threshold for source removal to $ML = 5.0$ increases the background level by only 1%. Within each band we generate a random number of events based on the Poisson statistics of the underlying background map for each pixel. The background contains non X-ray background (e.g., charged particles hitting the detector), unresolved X-ray sources, and possible diffuse X-rays. Our procedure thus may overestimate the real background counts, because the simulated sources contain those that are below the detection threshold as well. However, the contribution of these sources to the background is negligible compared to the input background counts. The energy channel of the event is selected by randomly assigning an energy within the limits of the band. No further consideration is made for the energy channel distribution within each band.

This is justified by the fact that the simulated data are only intended for testing source detection based on images from event files in these particular energy bands.

We have generated five different simulated data sets. Each has a different value for the individual rotations around the center of each observation and different (randomized) source and background counts.

4.2 Source Detection Algorithm

4.2.1 Processing Chandra data with XMM-Newton software

The Chandra CIAO software package does not provide a source detection algorithm that models the widely different PSF sizes and shapes of each source in multiple, overlapping pointings. We therefore use a PSF fitting code (`emldetect`), based on the XMM-Newton Science Analysis System (SAS; Gabriel et al. 2004), which performs simultaneous (joint) Maximum Likelihood fits of each candidate sources on sets of input images from several overlapping observations and in multiple energy bands, accounting for the appropriate PSF model in each case. A version of this code for use with Chandra data was originally created by one of the co-authors (H. Brunner) to perform source characterization in the Chandra COSMOS field (Puccetti et al. 2009). In addition to replacing XMM-Newton-specific calibration files with suitable Chandra equivalents, the XMM-Newton code was modified to account for the different azimuthal behavior of the Chandra PSF, as compared to XMM-Newton, resulting from the Chandra optical system. In the context of this work, we further improve and fine-tune this code. Note that the Chandra-emldetect code is not part of the XMM-Newton SAS provided by the XMM-Newton Science Operations Centre.

We also make use of the `eboxdetect` (sliding window source detection) and `esplinemap` (spline background-fitting of source-free image area) programs of the XMM-Newton SAS to create input candidate source lists which are to be an input for the `emldetect` PSF fitting code (details on these procedures are given in Watson et al. 2009). These XMM-Newton SAS programs do not require modifications to work on Chandra data. For compatibility with the XMM-Newton detection software, we create exposure maps (both vignettted and non-vignettted) and detection masks for each of the Chandra/AKARI NEP observations in the required XMM-Newton format. Specifically, the Chandra exposure maps as created by the CIAO package are converted from units of $\text{cm}^2 \text{ s ct ph}^{-1}$ to units of s to account for the different conventions of the Chandra and XMM-Newton software packages. XMM-Newton compatible detection masks, which indicate the area of each exposure on which source detection will be performed, are derived from the respective exposure maps.

4.2.2 Workflow of the Source Detection Algorithm

The XMM-Newton source detection program chain consists of three detection steps. We apply the same sequence of steps to both simulated and real data. First a sliding window detection using local background adjacent to each source is performed (`eboxdetect` local mode). The resulting initial source list is used to create background maps by performing

² <http://space.mit.edu/cxc/marx>

spline fits `esplinemap` to the source-free area of each image. A second sliding window detection run, making use of the spline fit background (`eboxdetect` map mode), creates an improved source list with a very low detection threshold. This catalog serves as input source candidate list for PSF fitting with `emldetect`. The reader is referred to the SAS manual³ for details.

4.2.2.1 Details on the individual source detection steps Making use of our simulated data sets, we explored several variations of this detection strategy. The approach found to achieve best results is described below.

eboxdetect (local mode): As some of our observations are rather short, the correspondingly small number of background counts in the area adjacent to each source does not permit us to determine the background level to sufficient accuracy. Therefore, we perform the initial detection on summed images, containing the photons from all observations. The three energy bands are kept separate, however, to increase the detection significance of very soft or very hard sources which only are detected in some of the energy bands.

esplinemap: For each observation, background maps in each energy band are created by performing spline fits to the area outside of a source cutout radius of 20 arcsec around each source. Although the simulated data sets are generated by using background maps and adding sources (see Section 4.1), we treat the simulated data identically to the real data. Thus, only the sources detected by the previous `eboxdetect` (local mode) run are excluded in this step.

eboxdetect (map mode): Making use of the spline fit background maps, this detection step is again performed on the summed images. Depending on the specific simulated data set used, 600–700 simulated sources with at least four counts lie within the survey region. We aim to find the detection threshold for `eboxdetect` such that the output source list (of `eboxdetect`) contains at least one entry for each of these simulated sources. The resulting list of *candidate* sources that fulfills this criterion contains more than 6000 entries. The task of `eboxdetect` (map mode) is only to detect the simulated sources (as completely as possible), before passing the candidate list to the next work step (`emldetect`) which performs the final PSF fitting and determines the final maximum likelihood value for each source. Only a few hundred sources will be above our specified final `emldetect` threshold. Creating a candidate list of more than 6000 entries ensures that we do not introduce a bias in the source selection.

emldetect: This task performs Maximum Likelihood PSF fits for each candidate source from the map mode `eboxdetect` list. Each source is fitted jointly (simultaneously) in each energy band of each overlapping pointings, using the appropriate PSF model in each case. The PSFs from the *Chandra* library are transformed into the format required by the *XMM-Newton* software. As the *Chandra* PSFs are provided on a two-dimensional positional grid, while the *XMM-Newton* PSF is calibrated as a function of off-axis angle, the *Chandra* PSFs are averaged over all azimuthal angles and the *XMM-Newton* software was modified such that the

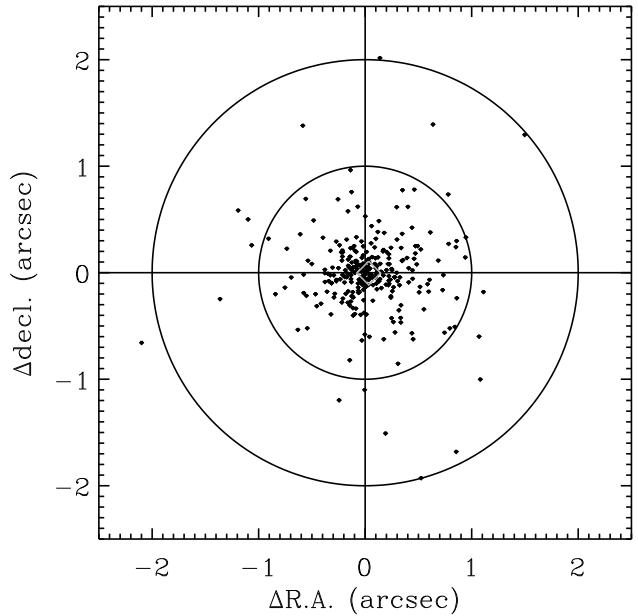


Figure 3. Comparison between input simulated source position and `emldetect` source position using a matching radius of 2.5 arcsec. The individual sources are shown as black diamonds. The median offset is represented by the gray diamond. The solid vertical and horizontal line indicate zero shifts in R.A. and decl. The black circles have radii of 1 and 2 arcsec. The sources shown here are above the internal $ML = 9.5$ source detection threshold.

PSFs will be rotated into the correct orientation for each detector location. We investigated whether the number of fit iterations is related to the accuracy with which the source counts and position are recovered, but do not find any such dependence.

The `emldetect` routine offers the possibility to fit the count profile of extended sources. Since our primary scientific focus is the detection of point-like sources, however, we do not make use of this option. Visual inspection of the X-ray images (see Figure 2) reveals only two obviously extended sources (visible as extended red objects). Moreover, the option to jointly fit the overlapping PSFs of neighboring sources is not used. Due to the relatively small PSF of *Chandra* this option was not deemed necessary. Note that even without the simultaneous fitting option, weak sources in the wings of brighter sources are handled correctly by first fitting the brighter source and including it in the background of the subsequent fit of the weaker source.

4.2.2.2 Running the source detection a second time

Our first-guess background maps were based on a source catalog produced by the local mode `eboxdetect` run. These initial background maps do not correspond to those used for our final `emldetect` run. However, a change of the background maps also affects the number of detectable sources. Thus, we rerun all routines of the source detection with the same parameter settings, but this time use the new source list as an input for the `esplinemap` routine to generate more sophisticated background maps.

4.2.2.3 Improvements over previous versions of the code

We implement two improvements in the `emldetect`

³ <http://xmm.esac.esa.int/sas/current/doc/packages.All.html>

code over the version used by Puccetti et al. (2009). First, Puccetti et al. (2009) (see their Figure 6) reported a small systematic shift between the median input and detected positions. We discovered that the *Chandra* PSF from the library was improperly adjusted to the individual observations. This caused a shift of the detected source position of up to 0.25 arcsec. While this error was also included in the original *XMM-Newton* version of the code, due to the smaller PSF, it is more apparent in the *Chandra* data⁴. After the correction of the error, (Figure 3) the remaining positional offset is only caused by statistical effects ($\Delta R.A.=0.03$ arcsec and $\Delta decl.=0.00$ arcsec; 288 objects).

For the PSF-fitting, the previous version of the *Chandra* `emldetect` code only considers counts from pixels that fall within a fixed radius from the `eboxdetect` position. We modified the code so that the relative fraction of the PSF that should be used for the fitting can be specified. We run extensive tests with a fit area corresponding to 50, 60, 70, 80, and 90 per cent of the individual PSFs in each input image. All runs give very similar results. We decide to use a fit area of 80 per cent of the PSF. Figure 4 shows the comparison between the old and new version, and demonstrates the significant improvement in recovering the correct source counts. The scatter visible in Figure 4 (right panel) can be explained by only the combination of the discrete probability of the number of input photons that are covered within the 80 per cent area of the total PSF and the statistical uncertainty of the background.

Puccetti et al. (2009) use a candidate source list based on the `PWDetect` code (Damiani et al. 1997) as input for their `emldetect` run. We also test this code and the CIAO task `wavdetect` (Freeman et al. 2002). We cannot generate a satisfying candidate source list in either case. In contrast to the *Chandra* COSMOS survey with ~ 50 ks mean exposure per pointing, our survey has pointings as short as 12 ks. The very low number of counts in these pointings most likely prevents the generation of useful catalogs of source candidates despite different parameter configurations. The `eboxdetect` algorithm, which works jointly (simultaneously) on all observations, creates an acceptable candidate source list.

4.2.3 Normalized Likelihood Values

The PSF-fitting program `emldetect` expresses detection likelihoods as normalized likelihoods, ML_2 , corresponding to the case of two free parameters, to permit comparison between different detection runs with different numbers of energy bands:

$$ML_2 = -\ln(1 - \Gamma(\frac{\nu}{2}, ML')) \quad \text{with } ML' = \sum_{i=1}^n ML'_i \quad (1)$$

where Γ is the incomplete Gamma function, n is the number of energy bands, $ML'_i = \Delta C_i/2$ where ΔC is the difference of the C -estimator as defined by Cash (1979) with respect to the null-hypothesis (i.e., zero source count-rate in the i -th band), and $\nu = 2 + n$ is the number of degrees of freedom of

the fit. The latter accounts for the fact that the number of degrees of freedom consists of two spatial coordinates plus the source count rates in each energy band.

ML_2 is related to the probability, P , of obtaining a detection likelihood of ML_2 or higher under the null-hypothesis (P-value) via $ML_2 = -\ln(P)$. The likelihoods are normalized to two free parameters, as these values yield a simple relationship to values of P . See the *XMM-Newton* SAS documentation⁵ for further details.

In Section 4.2.5, we obtain the effective detection likelihoods in the 2–7 keV band by numerically solving the above relation for ML' for both the 2–4 keV and 4–7 keV single band detection likelihoods ($n = 1$, $\nu = 3$). These are then added and an effective likelihood for the summed band, using the above relation ($n = 2$, $\nu = 4$), is computed. Hereafter, we refer to ML_2 simply as ML .

4.2.4 Calibrating the Normalized Likelihood

The implied probability from the maximum likelihood method calculated by the `emldetect` program may deviate from the actual false detection probability. This is the case when dealing with extremely low background and/or overlapping fields. In addition, a source detection run can be performed in a single energy band (e.g., 0.5–7 keV) or in multiple subbands covering the same total energy range (e.g., three band: 0.5–2, 2–4, 4–7 keV). The normalization of ML to two free parameters leads to different ML values for these two source detection scenarios. Thus, the ML -threshold used for `emldetect` should always be calibrated to the same spurious source detection rate by using simulated data.

To determine the best choice of ML , we start by running the source detection algorithm on our simulated data sets with a very low maximum likelihood threshold of $ML = 3$ for the `emldetect` routine. Different numbers of energy bands and energy ranges are applied: three bands over 0.5–2, 2–4, 4–7 keV, one band over 0.5–7 keV, one band 2–7 keV. We cross-identify sources in the simulated input catalog (all objects having at least four source counts) with the generated `emldetect` source catalog. As a first step, we simply apply a 2.5 arcsec matching radius. In Sect. 4.3.1, we will describe how we optimize this cross-identification. A detected source is considered spurious if there is no simulated input source within a 2.5 arcsec radius. Since the probability that a spurious source falls within the matching radius of a simulated input source position is very small, we regard all detected sources that have a counterpart in the simulated catalog as true counterparts. We justify this assumption by finding only up to two sources with counterparts in the simulated catalog when we shift all detect sources by 30 arcsec in R.A. direction.

We derive the number of overall detected sources (true counterpart plus spurious sources) and the number of false (spurious) detections with increasing ML threshold for each simulated data set. Figure 5 shows the average of two simulations considering the three-band (0.5–2, 2–4, 4–7 keV) and full-band (0.5–7 keV) source detection runs. We verify the expected finding of having more detected sources at low

⁴ The error has been corrected in current versions of the *XMM-Newton* SAS software package.

⁵ <http://xmm.esac.esa.int/sas/current/doc/emldetect>

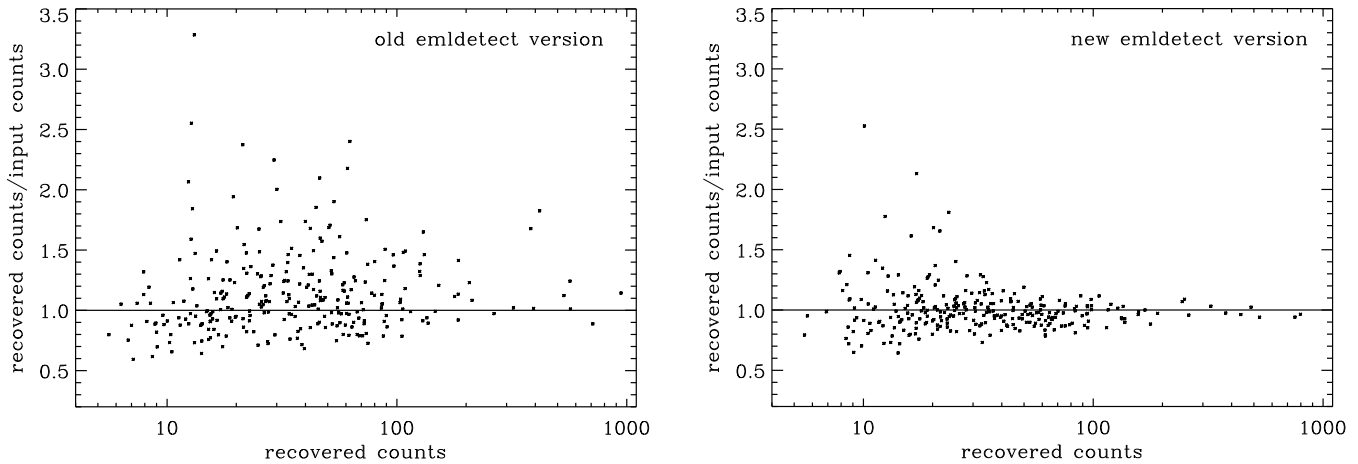


Figure 4. Comparison between the old and new versions of *emldetect*. The plots show the ratio between the best-fit recovered counts and the simulated input counts vs. recovered counts. The old version used a fixed radius of 7 pixels (~ 3.5 arcsec) for the PSF-fitting, while the new version applies the fit to all counts within an area of 80 per cent of the PSF. Both runs use an internal $ML = 9.5$ threshold. All other parameters are identical.

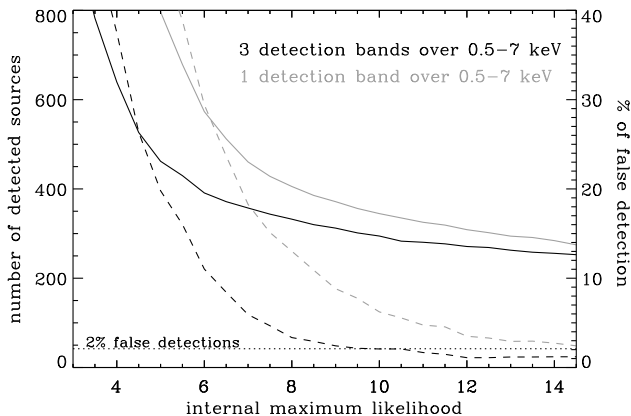


Figure 5. Number of overall detected sources (solid lines; left y-axis) and fraction of false (dashed lines; right y-axis) detections as a function of internal maximum likelihood threshold value used in the source detection algorithm. To cross-identify the recovered sources with the simulated input sources, we use a simple 2.5 arcsec matching radius.

ML values and also a high fraction of spurious detections. With increasing ML values, the fraction of spurious detections decreases significantly. Both methods reach the same fraction of spurious sources at different ML values. When we apply the same source detection scenario to different simulated data sets, the fraction of spurious detection varies by ± 1 per cent at the same ML -value. We find differences of up to 8 per cent (median 4 per cent) in the number of total detected sources (simulated input and spurious sources) between the simulated data sets (at the same ML -value).

The primary goal is to aim for a secure X-ray source catalog in the *Chandra*/*AKARI* NEP deep field that has a spurious source detection rate of ≤ 2 per cent. Using the simple cross-identification criterion, we meet this goal at approximately $ML \sim 9.5$ for the source detection run with three energy bands and $ML \sim 14.5$ for the single 0.5–7 keV band run, respectively (see Figure 5). At the same spurious

source detection rate, the source detection run over three subbands covering 0.5–7 keV reveals ~ 5 –10 per cent more simulated input sources than the run with one band over the same energy range. Hence, the three subband method is preferred over a source detection using a single energy band image. We compare both methods in respect to differences in their detected sources in Appendix A in more detail.

We also determine the ML -threshold for a source detection run in only the 2–7 keV band. In this band, we reach a spurious source detection rate of ≤ 2 per cent at $ML \sim 12.0$.

4.2.5 Final Source Catalog

After determining the ML -threshold for different source detection runs, we are now in a position to construct our catalog using the following steps.

Since we are interested in all sources that originate from source detection runs with a spurious source detection rate of ≤ 2 per cent, we consider objects from a detection runs in three subbands (0.5–2, 2–4, and 4–7 keV) and of source detection runs using a single band of 0.5–7 or 2–7 keV. The simulated data sets serve as a guideline for the optimal source catalog construction.

We construct a primary catalog from the joint (simultaneous) source detection run in three energy subbands. We justify this by the fact that this run detects more sources than any other source detection run in a single band. A source will be listed in the catalog if the total maximum likelihood over all three bands is above $ML = 9.5$ (Eq. 1; spurious source detection rate of ≤ 2 per cent).

We test different approaches as to how to find additional “soft”, “medium-hard”, and “hard” sources that escaped detection in the joint (simultaneous) three subband detection run covering 0.5–7 keV. All additional sources make up only a small fraction compared to the primary catalog. However, some approaches add also a large number of spurious sources. Thus, our main criterion is that we do not significantly degrade our reliability of the final source catalog by adding a relatively small number of objects.

As the first step, we generate a source list that uses the same sophisticated background maps as for the final source detection run with an `emldetect` threshold of $ML = 9.5$ in either the soft band or the combined hard band (i.e., 0.5–2 and 2–7 keV), while setting the all-three-combined threshold to a very low value of $ML = 5$. All other source detection parameters and input data are not changed. We choose a combined $ML = 5$ to detect all sources that might have $ML \geq 9.5$ in a single subband but still $ML < 9.5$ in the combined 0.5–7 keV band. Using even lower combined ML -values does not add any additional sources to the final source catalog.

Additional soft and medium-hard sources: To extract additional soft energy sources, we now select only sources that have a maximum likelihood $ML \geq 9.5$ in the 0.5–2 keV band. We verify with the simulated data sets that most of these sources will already have an entry in the primary catalog. Typically only ~ 20 objects are added to the primary catalog.

We also add all sources with a maximum likelihood $ML \geq 9.5$ in the 2–4 keV band. On average, this adds two sources that have also counterparts in the simulated input catalog. We do not consider sources from the 4–7 keV subband, as our simulated data sets show that all of these source (which have not been detect in the three subband run or in another subband) are spurious.

Additional hard sources: Based on the catalog with the threshold of $ML = 5$, we use the ML values of the 2–4 and 4–7 keV bands to calculate a combined 2–7 keV maximum likelihood (see Section 4.2.3). All sources that are above a combined 2–7 keV $ML = 9.5$ are added to the primary catalog. Evaluating the source detection runs on our multiple simulated data sets, this procedure only finds between 1 and 3 additional objects. Consequently, the final source catalog contains all objects that have $ML \geq 9.5$ in either the combined three energy bands, soft band, or hard (2–7 keV) band.

Additional sources from single-energy source detection runs: Finally, we examine objects from a source detection run in one band over 0.5–7 keV ($ML \geq 14.5$) and in one band over 2–7 keV ($ML \geq 12.0$). The vast majority of objects that are not included in any other source detection run are at the far edges of our *Chandra* observation. Both source detections together would add 7 to 8 sources to the final source catalog based on our simulated data sets. Comparing the detected sources to the simulated input catalogs also shows that up to 50% of the additional sources are spurious. Therefore, we only add these additional sources to our final source catalog if they fall within the area covered by our deep Subaru imaging data. At the end, this method adds between 1 and 3 additional simulated sources (based on different simulated data sets) that have not been detected by any other source detection run. On average, more additional sources are found in the 0.5–7 keV than in the 2–7 keV detection run.

To achieve a consistent final source catalog, we use the position of the objects of the single-band detection and identify the corresponding counterpart in the source detection run over three subbands with a combined $ML = 5$ threshold. All sources have counterparts. We use these (combined $ML = 5$) fluxes, likelihood values, hardness ratios, and the position for the final source catalog. Only for the band in

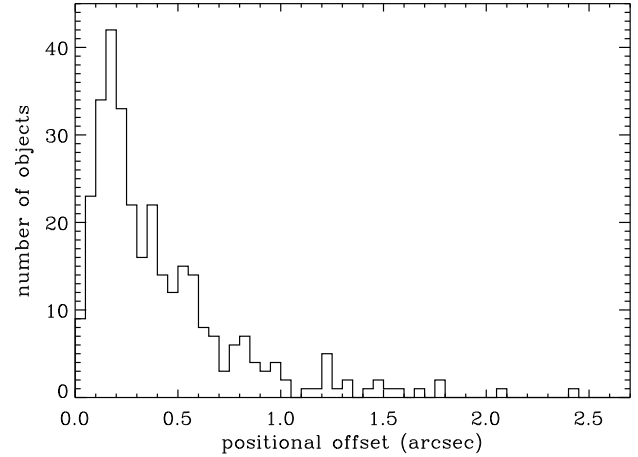


Figure 6. Number of recovered input sources vs. offset between recovered position and input position when using a simple 2.5 arcsec matching radius. The plot shows a simulated source detection run with an internal maximum likelihood threshold of $ML = 9.5$.

which these additional sources are detected, we employ the single-band detection run counts, count rate, and fluxes in the final source catalog.

4.3 Characterizing the Quality of the Source Detection Algorithm

After optimizing the source detection algorithm by using simulated data, we can now explore the quality of the resulting source catalog by investigating the distribution of position errors, completeness and overall maximum likelihood.

4.3.1 Distribution of Position Errors

In the last subsection, we used a very simple approach to cross-identify sources between the simulated input catalog and source detection catalog. This is not optimal, as the position of each individual source has its own systematic uncertainty. Since we know the location of the input sources, we can explore the best-suited method to cross-identify the final X-ray sources with their counterparts. The optimal method maximizes the number of true cross-identifications while minimizing, or even excluding completely, wrong counterpart identifications. This will be very valuable knowledge as we have to determine the optical/IR counterparts of our real data X-ray sources without knowing the exact matches a priori.

We study the distribution of the positional offsets between the original and recovered sources cross-identified with a simple ≤ 2.5 arcsec separation. Figure 6 shows the distribution of positional offsets between simulated input and final source catalog in units of arcseconds. Ninety per cent of all sources have counterparts within 1.0 arcsec. We inspect the sources that have offsets of 1.0 to 2.5 arcsec between the input and recovered output positions. For these objects, we verify by visual inspection that they are the correct cross-identifications. If we restrict ourselves to the area covered by the deep Subaru imaging, we are left with only 5 sources with offsets between 1.0 to 2.5 arcsec (instead of 21 objects).

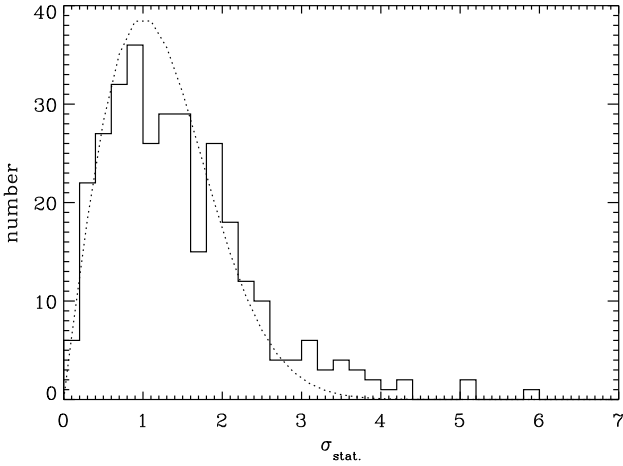


Figure 7. Number of objects identified as simulated input sources vs. positional error in units of $\sigma_{\text{stat.}}$. The objects shown here (solid line) are the same as in Figure 6. The dotted line represents the theoretical expectation for a two-dimensional Gaussian distribution.

All these offsets can be explained by point-like objects with a low number of source counts, where the individual counts are in an extended or non-radial distribution. These particular source count distributions cause a challenge for the source detection algorithm to recover the correct input position.

Considering all objects that can be cross-identified with a simple 2.5 arcsec radius and normalizing the positional offsets with their individual positional error results in Figure 7. The measured distribution does not agree well with a two-dimensional Gaussian distribution of the positional offset. We have a significant number of true counterparts that require matching radii of more than $2.5\sigma_{\text{stat.}}$. This can be explained by our assumption that the uncertainties of the position follow a Gaussian distribution. However, the source detection routine fits a PSF to a source to determine the position. A PSF can have very wide wings, much wider than in a Gaussian distribution. We suspect that the distribution in Figure 7 can be described by the sum of a Gaussian and a much wider spread distribution which produces the tail towards large $\sigma_{\text{stat.}}$.

Excluding the outer regions of our survey by only considering the deep Subaru imaging area reduces significantly the number of objects that require large matching radii. In order to correct for the non-Gaussian distribution we add a 'systematic uncertainty' of $\sigma_{\text{sys.}} = 0.1$ arcsec quadratically to the statistical position errors. We choose this value as we do not want to significantly misalign the peaks between theoretical and observed distribution. Furthermore, we want to keep the summed area of all individual positional error circles as small as possible. To include all correct cross-identifications, we test different maximum positional offset (units of σ). We obtain a satisfying agreement when using $\sigma_{\text{total}} = 5 \times \sqrt{\sigma_{\text{sys.}}^2 + \sigma_{\text{stat.}}^2}$ with $\sigma_{\text{sys.}} = 0.1$ arcsec.

We rerun the cross-identification with this optimized procedure instead of using a simple 2.5 arcsec radius. The resulting distribution of positional offsets using our optimized procedure is shown in Figure 8. Only the deep Subaru imaging area is considered. A fraction of ~ 80 per cent of all recov-

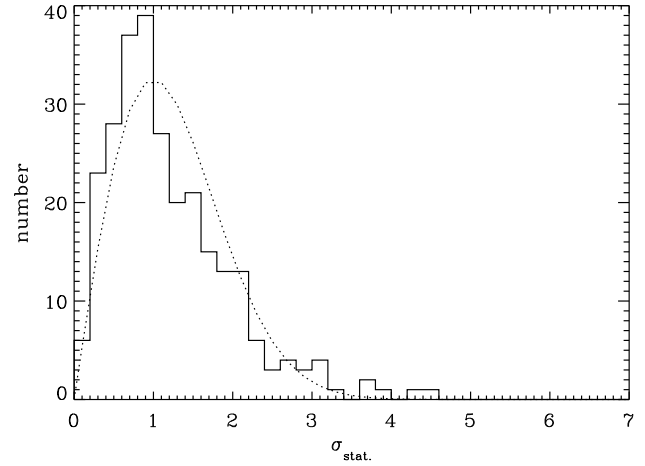


Figure 8. Similar to Figure 7. Here we apply our final matching criterion of $\sigma_{\text{total}} = 5 \times \sqrt{\sigma_{\text{sys.}}^2 + \sigma_{\text{stat.}}^2}$ with $\sigma_{\text{sys.}} = 0.1$ arcsec. Only sources within the deep Subaru imaging region are considered. An internal threshold of $ML = 9.5$ has been used for the source detection run.

ered X-ray sources have their input position within $2 \times \sigma_{\text{total}}$, while ~ 95 per cent have counterparts within $3 \times \sigma_{\text{total}}$.

We verify that the new cross-identification criterion also correctly recovers the simulated input sources. The new cross-identification method reduces the area that has to be considered for all counterparts in the deep Subaru imaging region by a factor of ~ 2.5 compared to the 2.5 arcsec matching radius. Consequently, we significantly reduce the probability that a random (X-ray unrelated) source is selected as the corresponding X-ray counterpart. This is of utmost importance, considering the high number density of optical sources in the deep Subaru images.

4.3.2 Completeness

We study the completeness (fraction of recovered sources over number of simulated input sources) as a function of input counts (Figure 9) for the final source catalog. We only consider all simulated input sources which have at least four counts in the total (added) observation as counterparts. This restriction is justified by using the simulated data sets; a source detection with a spurious source detection rate of ≤ 2 per cent is only sensitive to detect sources with four or more counts in the simulated input catalogs.

For objects with four counts, we are, averaged over all simulations, complete to 51 per cent. We are above the 80 per cent completeness level for all sources that have more than seven input counts, while we detect objects with at least 15 counts with a completeness fraction of 95 per cent. However, these numbers are averages over the whole field. Especially in the outer region of the *Chandra* observation, the completeness is reduced, since at these large off-axis angles the source counts are distributed over larger areas and have less observation time than the central areas. This makes it more difficult for the source detection algorithm to correctly recover the input sources. If we restrict the area only to the region covered by the Subaru imaging data, the completeness is ~ 3 per cent higher for all objects. Therefore, in

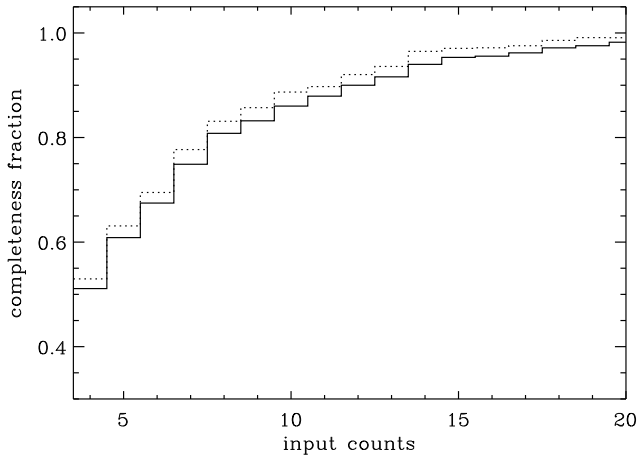


Figure 9. Completeness fraction as a function of simulated input counts when using an internal maximum likelihood threshold of $ML = 9.5$. The solid line represents the completeness for the whole *Chandra* observation, while the dotted line considers only sources that are covered by the deep Subaru imaging data.

this region we already reach a completeness level of 95 per cent for sources having more than 13 counts.

4.3.3 Estimating the Overall Maximum Likelihood Value

Since the maximum likelihood threshold used by the `emldetect` program deviates from $ML = -\ln(P)$ (see Section 4.2.4), the true underlying maximum likelihood for our survey has to be determined from the number of spurious sources. Given that the number of spurious sources and the number of simulated data sets are small, we will refer to this value only as empirical maximum likelihood value. As our primary scientific interest is the area in which we also have deep Subaru imaging, the calculations below only refer to this area. We estimate the value ML_{empir} by computing the number of false sources per independent PSF detection cell using the following steps.

The source detection runs on the simulated data sets with an internal threshold of $ML = 9.5$ contain on average four to five spurious detections (~ 1.7 per cent), e.g., sources that are not associated with any simulated input sources.

We determine the FWHM of the averaged PSF (in the summed observation) of approximately 50 randomly selected sources (across the whole deep Subaru imaging field, bright and faint sources). Since the vast majority of the sources are detected in multiple observations at various off-axis positions, the sizes of the combined PSFs are rather similar. The x- and y-FWHM components of the averaged PSF are 5.9 and 4.1 pixels, respectively. We also determine the total number of pixels that are covered by our detection maps in the deep Subaru imaging area (~ 13.18 million square pixels). Dividing the area of the total detection area by the area of the average FWHM (~ 19 square pixel) yields an estimate of the number of independent detection cells.

Using the final source catalog based on simulated data sets results, on average, in four spurious detections. Consequently, we determine the probability that a detection cell contains a spurious detection to be $P = 5.7 \times 10^{-6}$. This probability corresponds to the (empirical) maximum likeli-

hood value of $ML_{\text{empir}} = 12$. This translates into a 4.4σ detection. Adding or subtracting one more spurious source only marginally changes ML_{empir} by $\Delta ML_{\text{empir}} = \pm 0.2$.

We will refer in this paper to the 'maximum likelihood value' (ML_{empir}) when we talk about the empirical value and to the 'internal ML value' whenever we refer to the value used for the `emldetect` routine as threshold for the source detection run over three subbands.

Only considering the the area outside the deep Subaru imaging (area of large off-axis angles in our *Chandra* pointings) the empirical maximum likelihood value drops to $ML_{\text{empir}} \sim 10.7$.

5 REAL DATA PRODUCTS

With an optimized source detection algorithm, cross-identification procedure, and knowledge about the accuracy of recovering the number of photons, we are now in a position to generate the real data source catalog.

5.1 Astrometric Correction of the Individual Observations

Before we run the source detection algorithm on the (real) observations, we process all the individual observations separately to check how well they are astrometrically calibrated. As the Subaru/Suprime-Cam is used as the astrometric reference frame in the *AKARI* NEP deep field, we astrometrically calibrate the *Chandra* observations to the same standard.

In each observation, We run a joint source detection in the 3 subbands covering 0.5–7 keV with an internal threshold of $ML = 10$. The number of detected sources in each individual observation is given in Table 1 in column “#sources ($ML \geq 10$)”. Then, we positionally cross-correlate Subaru z' -band detections with $m_{z'} < 23.5$ with the detected X-ray sources that are within an off-axis angle of 7 arcmin.

The magnitude cut used in the Subaru z' -band catalog is determined from the measured distribution of X-ray and optical counterparts after merging all individual *Chandra* observations. Shifting the X-ray sources by ± 40 arcsec, we detect a significant increase of spurious counterparts above this limit. At $m_{z'} < 23.5$, we estimate a spurious counterpart identification rate of less than 4 per cent. We only consider X-ray sources with off-axis angles of less than 7 arcmin as the PSF significantly broadens, i.e., the radius which encircles a specified fraction of total counts increases. At 1.5 keV and an off-axis angle of 7 arcmin, 50 per cent of the enclosed counts fraction is still within ~ 3 arcsec. The area that encloses 50 per cent of all counts doubles when going from 7 arcmin to 10 arcmin. We therefore restrict ourselves to 7 arcmin to balance between having enough objects for a proper cross-identification and significantly reducing the uncertainties on the positions.

We then derive the offset in R.A. and decl. for each object in consideration (this results in a plot similar to Figure 3). For the final offset calculation, which is used for correcting the event lists and aspect solution, we only consider counterparts that are within a 1 arcsec radius from the average offset position. This ensures that only very secure cross-identifications are used for the astrometric correction.

The number of objects that determine the final offset value is given in Table 1 in column ‘#offset’. A rotation or/and scaling factor are not needed to improve the matching of X-ray and optical sources. We therefore correct the event lists and the aspect solution file only by the positional offset given in Table 1 columns “ Δx ” and “ Δy ”.

The remaining positional uncertainty in the astrometric calibration (quadratically adding Δx and Δy) is less than 0.2 arcsec compared to the Subaru z' -band catalog. Changing the z -band limiting magnitude by ± 0.5 mag and the off-axis angle limit by ± 2 arcmin changes the offset correction by less than 0.1 arcsec in each individual observation. The final source detection algorithm uses the astrometrically corrected data products.

5.2 Main Source Catalog

The source catalog uses an internal threshold of $ML = 9.5$ which corresponds to $ML_{\text{empir}} \sim 12$ (see Sect. 4.3.3). In total, 457 sources are detected, of which 377 objects fall in the deep Subaru imaging region. This catalog is designed to *identify* X-ray emitting objects in the *Chandra*/*AKARI* NEP deep field. Together with the optimized cross-identification procedure, the clear advantage of the catalog is the very high reliability, while the catalog sacrifices completeness for objects with low counts (see Figure 9). Only ~ 1.7 per cent of the objects listed in the source catalog are expected to be spurious source detections.

Considering the uncertainty in the astrometric calibration, all sources should be considered as possible X-ray counterparts that are within a radius of $r_{\text{match}} = \sqrt{\sigma_{\text{total}}^2 + \sigma_{\text{astro}}^2}$ with $\sigma_{\text{total}} = 5 \times \sqrt{\sigma_{\text{sys.}}^2 + \sigma_{\text{stat.}}^2}$ and $\sigma_{\text{sys.}} = 0.1$ arcsec and $\sigma_{\text{astro.}} = 0.2$ arcsec (astrometric uncertainty). For all sources within the deep Subaru imaging region ($\sim 3.2 \times 10^6$ arcsec²), the area $A = \pi r_{\text{match}}^2$ adds up to ~ 2970 arcsec². This quantity can be used to calculate the expected number of spurious source identifications based on the source density of the catalog for which we seek identifications.

5.2.1 Description of Source Catalog

The catalog is available as a table (FITS format) from the VizieR Catalogue Service website⁶. In the following, we will describe the columns in the table. First we list the number of the column, followed by the name, its unit, and description. The values given in columns 2–4 are based on the primary source catalog (three energy band images covering 0.5–7 keV), unless the source is only detected in the soft (0.5–2 keV) or the hard (2–7 keV) energy band.

- 1) column#1: **CID** — unit: none — *Chandra* source identification number
- 2) column#2: **RA** — unit: deg — right ascension of the source position
- 3) column#3: **DEC** — unit: deg — declination of the source position
- 4) column#4: **RADEC_ERR** — unit: arcsec — statistical error $\sigma_{\text{stat.}}$ of the source position calculated by combining the

1σ statistical uncertainties on the R.A. and decl. (unit: arcsec) following:

$$\text{RADEC_ERR} = \sqrt{\text{RA_ERR}^2 + \text{decl_ERR}^2}.$$

The values in this column do not include the additional systematic uncertainty to optimize the source detection (Sect. 4.3.1), nor do they contain the uncertainty of the astrometric calibration of the *Chandra* data to the Subaru/Suprime-Cam reference frame in the *AKARI* NEP deep field (Sect. 5.1). To determine the counterparts of our X-ray sources in other wavelength regimes, we recommend using the equation given in Sect. 5.2.

The next columns list the quantities in different energy bands in the following order: 0.5–7 keV (total band), 0.5–2 keV (soft band), 2–7 keV (hard band), 2–4 keV (medium hard band), and 4–7 keV (ultra hard band). Consequently, the column names are repeated and list the quantity in the corresponding energy band using the order given above. For example, the expression ‘column#9.16.23.30.37’ denotes that the flux in the 0.5–7 keV band is given in column #9, the flux in the 0.5–2 keV band in column #16, and so on. The `emldetect` routine corrects automatically all counts, count errors, rates, rate errors, fluxes, and flux errors for the PSF fraction size. Thus, these values do not correspond only to the used 80 per cent PSF fraction size, but represent the true (intrinsic) quantities.

- 5) column#5.12.19.26.33: **CTS** — unit: counts — source counts
- 6) column#6.13.20.27.34: **CTS_ERR** — unit: counts — 1σ uncertainty of source counts
- 7) column#7.14.21.28.35: **RATE** — unit: counts s⁻¹ — vignetting-corrected source count rate
- 8) column#8.15.22.29.36: **RATE_ERR** — unit: counts s⁻¹ — 1σ uncertainty of vignetting-corrected source count rate
- 9) column#9.16.23.30.37: **FLUX** — unit: erg s⁻¹ cm⁻² — source flux

Single energy conversion factors ECFs are used to convert observed count rates into observed fluxes (corrected for Galactic absorption), based on the instrumental response and an assumed spectral properties of the X-ray source. All ECFs consider the Galactic column density for the *AKARI* NEP deep field of $N_{\text{H,Gal}} = 4.0 \times 10^{20}$ cm⁻² and a power-law spectrum with a photon index of $\Gamma = 1.4$. The same photon index has also been used by other major *Chandra* surveys such as Kim et al. (2007) and Puccetti et al. (2009).

We also consider the time dependent degradation of the CCD response at low energies by using the time-averaged calibration files from *Chandra* cycle 12. Depending on the energy band used, OBSIDs 10443 and 11999 from cycle 10 have an up to 8 per cent higher sensitivity. To correctly account for this fact and use single ECFs for all observations based on cycle 12 only, we multiply the exposure maps of these observations by the corresponding correction factors. In other words, we normalize the cycle 10 exposure maps to cycle 12. Furthermore, we also investigate the issue that our observations have been obtained in the beginning of cycle 12, while our analysis uses the averaged calibration data from the whole of cycle 12. Comparing the average instrument response (count to flux conversion) of cycle 11 with that of cycle 12 reveals the largest difference to be in the

⁶ <http://vizier.cfa.harvard.edu/>

lowest energy band (0.5–2 keV). However, the discrepancy is only 2 per cent, and will not significantly contribute to the flux uncertainties.

The ECFs used for the 0.5–2, 2–4, 4–7, 2–7, 0.5–7 keV energy bands are: 1.523, 0.704, 0.344, 0.509, and 0.849, respectively (count rates to fluxes in units of 10^{-11} erg s $^{-1}$ cm $^{-2}$). One limitation of using a single ECF is that the flux is only correct if each object has the same spectral shape as assumed for the ECF calculation. Changing the photon index from $\Gamma = 1.4$ to $\Gamma = 2.0$ decreases the flux, e.g., by ~ 20 per cent for the same number of detected photons in the 0.5–7 keV band.

Assuming the same photon index of $\Gamma = 1.4$ the Galactic absorption corrected flux can be converted to a flux ($N_{\text{H,Gal}}$ -corrected) in different bands (e.g., 0.5–2 keV to 0.2–2 keV: multiply by 1.33; 2–7 keV to 2–8 keV: multiply by 1.16; 2–7 keV to 2–10 keV: multiply by 1.45).

10) column#10.17.24.31.38: **FLUX_ERR** – unit: erg s $^{-1}$ cm $^{-2}$ – 1σ uncertainty of the source flux)

If a source is not detected in an energy band (internal *ML*-threshold in this energy band below 9.5), we list the upper 90 per cent limit (see Sect. 5.4) as the flux error. We make such cases visible by giving it a negative value in the **FLUX_ERR** column and setting the flux (**FLUX**) to zero. The two sources that have a *ML*-threshold in the 0.5–7 keV band below 9.5 originate from a 0.5–7 keV single band source detection run. To quote similar *ML* values for all objects we list the total 0.5–7 keV *ML* values from the joint three energy band source detection run. The listed counts, count rates, fluxes, and the corresponding uncertainties in the 0.5–7 keV band are taken from the single band detection run.

11) column#11.18.25.32.39: **ML** – unit: none – internal maximum likelihood $ML = -\ln(P)$ of the source detection derived from **emldetect** (see Sect. 4.3.3 and appendix on the interpretation of these values)

12) column#40: **HR_soft_hard** – unit: none – hardness ratio in the 0.5–2 keV and 2–7 keV energy bands

The hardness ratio, equivalent to a color index in the optical, is the simplest way to characterize an X-ray spectrum. The count rates in two energy bands are used to compute the hardness ratio by $HR = (RATE_B - RATE_A)/(RATE_A + RATE_B)$, where band A is the low and band B the high energy band. We use the count rate, instead of the source counts, for two reasons. Firstly, the count rate is one of the parameters that is fitted by the **emldetect** software, and is therefore a direct output. Secondly, the count rate is corrected for vignetting, while the source counts are not. In the case that a hardness ratio and/or its uncertainties are undefined (count rates in both bands are zero), the value 9999.0 is given in the table.

13) column#41: **HR_ERR_soft_hard** – unit: none – 1σ uncertainty of 0.5–2 keV to 2–7 keV hardness ratio

14) column#42: **HR_soft_med** – unit: none – hardness ratio of the 0.5–2 keV and 2–4 keV energy bands

15) column#43: **HR_ERR_soft_med** – unit: none – 1σ uncertainty of 0.5–2 keV and 2–4 keV hardness ratio

16) column#44: **HR_med_ult** – unit: none – hardness ratio of the 2–4 keV and 4–7 keV energy bands

17) column#45: **HR_ERR_med_ult** – unit: none – 1σ uncertainty of 2–4 keV and 4–7 keV hardness ratio

18) column#46: **IN_AREA** – unit: none – If the source falls within the deep Subaru/Suprime-Cam imaging region, we set this value to 1, otherwise 0.

5.3 Sensitivity Maps

One important quantity to know is the flux that would have caused a detection of a source at each position in the survey. This flux depends on the maximum likelihood threshold chosen in the source detection run, the point spread function, and the background level at the chosen position.

We create sensitivity maps in different energy bands by searching for the flux to reject the null-hypothesis that the flux at a given position is only caused by a background fluctuation. Ideally the detection threshold at a given position could be obtained by repeating the Maximum Likelihood fitting procedure to simulated images with the background and a source models with varying source count rates. This procedure is computationally prohibitive, and thus we take a faster approach of using Poisson probabilities as follows. In a chosen energy band, we determine for each position in the survey the flux required to obtain a certain Poisson probability above the background counts. Since $ML = -\ln(P)$, we know from our *ML* threshold the probability we are aiming for.

One major challenge in surveys with overlapping observations, such as the *Chandra/AKARI* NEP survey is the different contribution of each observation to the total detection likelihood of a source. We here develop a procedure to create the sensitivity map for the overlapped fields.

1) For each observation and for each band, we generate a PSF-summed background map, in which the value at each position is the sum of all background counts (generated by the spline fits; see Sect. 4.2.2) within r_{80} (80 per cent PSF encircled radius for the off-axis angle of the position). This radius is calculated from the *Chandra* PSF library. We use a circular area within r_{80} for smoothing with the PSF, since this is the region used for the Maximum Likelihood PSF fitting.

Consequently, pixels close to the optical axis in an observation end up with a lower PSF-summed background value than pixels at large off-axis angles. For pixels outside an individual observation, we check if they overlap with other observations and if their r_{80} overlaps with pixels of the chosen observation. If both conditions are met, the pixel outside the given observation is also assigned the sum over all pixel with a non-zero value within r_{80} .

2) Using the individual exposure maps in different energy bands, we create exposure maps that are smoothed by the PSF (PSF-weighted averaged exposure maps). Each pixel that falls within r_{80} is given a weight corresponding to its distance from the central pixel. The weights are determined from the shape and size of the azimuthally-averaged *Chandra* PSF, and are normalized such that the integral over all pixels in an area with r_{80} amounts to 0.8. This value accounts for the fact that an input count rate of 1 ct s $^{-1}$ will be spread out over r_{80} and results in a detection of only 0.8 ct s $^{-1}$. We multiply all exposure map values from pixels within r_{80} with the corresponding weight, add them, and divide them by the integral over all weights (0.8). The resulting PSF-smoothed exposure map will correctly recover

the true count rate even when only considering pixels within r_{80} .

For pixels that are outside an individual observation, we test if their r_{80} overlaps with pixels of the chosen observation. If so, we follow the same procedure as described above. These pixels will end up with lower exposure time because some pixels will have zero exposure, but their weights will still contribute to the overall normalization.

3) We finally search at each pixel position in the survey for the input flux value that results in

$$ML_{\text{threshold}} = -\ln(P_{\text{total}}) \quad \text{with } P_{\text{total}} = \prod_{i=1}^{\#obs.} P_i$$

where P_i is the probability, for the null hypothesis that the r_{80} region around the position is only contributed by the background, to obtain c_i counts or larger in the same region. This probability P_i for the given background b_i to produce an integer count c or more is the sum of the usual Poisson probabilities:

$$P_i(c) = \sum_{k=c}^{\infty} \frac{b_i^k e^{-b_i}}{k!}. \quad (2)$$

The value b_i is calculated by the counts in the background maps within r_{80} . If the source has an original count rate of CR , the expectation value for the source+background count is $c_i = CR \times t_{\text{exp},i} + b_i$, where $t_{\text{exp},i}$ is the PSF-weighted mean exposure value over r_{80} region (see above) for the observation i . The value of c_i is not necessarily an integer, and thus we cannot apply Eq. 2. Thus, we calculate $\ln P_i$ value by an linear interpolation between $\ln P_i(c)$ and $\ln P_i(c+1)$, where c is the largest integer that does not exceed c_i . In the calculation of c_i , we do not invoke a 4-count floor. Unlike the case of our 90 per cent confidence upper flux limits (Sect. 5.4), we do not use a Bayesian approach, since the ML-fitting procedure itself is based on the null-hypothesis probabilities.

For a given position, we consider all observations that have an individual PSF-smoothed exposure map value larger than zero. Our resulting flux limit of the sensitivity maps corresponds to the CR value that gives $-\ln P_{\text{total}}$ which equals our chosen $ML_{\text{empir}} = 12$ threshold. In practice, we search for a value of $-\ln P_{\text{total}}$ that falls within $\Delta ML = \pm 0.2$ of our targeted ML_{empir} threshold. This tolerance range corresponds to having one spurious source more or less in the whole survey. The accuracy of the sensitivity maps is tested by comparing input and output $\log N - \log S$ relations for the simulated data sets in Sect. 6.1. Note, that outside the deep Subaru/Suprime-Cam imaging the sensitivity maps should be used with caution since we assume for their generation a $ML_{\text{empir}} = 12$ over the whole area covered by *Chandra*.

All sensitivity maps in different energy bands are publicly available in FITS format on the VizieR Catalogue Service. Figure 10 shows the flux limit of our source detection as a function of area for the *Chandra*/AKARI NEP field that overlaps with the deep Subaru imaging data. We use the sensitivity map of the corresponding energy band and count the number of pixels below or equal the chosen detection flux limit. The number of pixels is then converted into an area. The plot shows that we are most sensitive in the 0.5–2

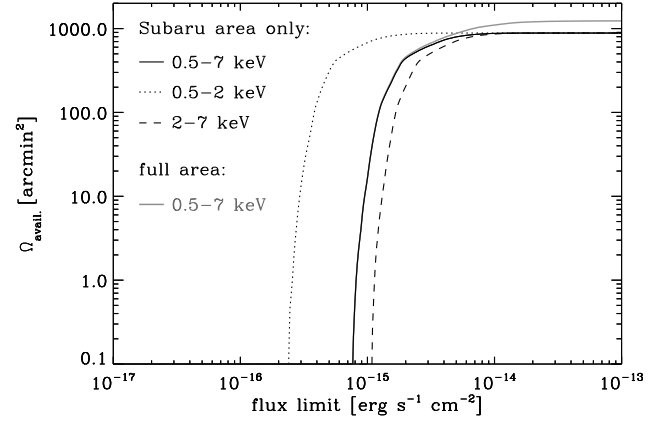


Figure 10. Sensitivity limit of our source detection vs. available solid angle for different energy bands. A source with a flux S can be recovered by our detection algorithm within the given available survey area. The plot is based on using a maximum likelihood threshold of $ML_{\text{empir}} = 12$.

keV band. The area covered by the Subaru imaging data is 885 arcmin^2 (total *Chandra* survey area: 1236 arcmin^2).

5.4 Flux Upper Limit Maps in Overlapped Mosaics

The 90 per cent confidence upper limit maps are computed in a similar way as the sensitivity map values (see Sect. 5.3). The difference is that we take a Bayesian approach following Kraft et al. (1991). Consequently, we obtain the 90 per cent confidence upper flux limit by searching for the flux such that *given the observed counts* the Bayesian probability of having this flux or larger is 10 per cent.

According to Bayes theorem, the posterior probability that the model (M) is right given the data (D) can be expressed by:

$$P(M|D) = \frac{P(D|M)P(M)}{\int P(D|M)P(M)dM}, \quad (3)$$

where the model M in our case is that the underlying count rate (i.e., true flux on the sky processed via the optical and detector systems) of the source is cr_{SRC} and the data (D) is that, this position of the sky is covered by N *Chandra* fields, indexed by i , each obtaining with observed c_i (integer) source+background counts, under the observational conditions that the PSF weighted (normalized to 0.8) effective exposure is $t_{\text{exp},i}$, and the background map count is b_i , all measured within the radius r_{80} of the source position (see Sect. 5.3).

Now we assume a prior distribution $P(M)$ that is constant in $cr_{\text{SRC}} \geq 0$. Since our background map has been obtained from the spline image, we ignore statistical fluctuations of b_i . For each field i , the model source count is $s_i = cr_{\text{SRC}} \cdot t_{\text{exp},i}$, and thus the probability of obtaining c_i counts under the model source + background counts $s_i + b_i$ is $P_{\text{pois}}(c_i, s_i + b_i)$, where $P_{\text{pois}}(\lambda, k) = \frac{\lambda^k}{k!} e^{-\lambda}$ is the Poisson distribution.

Then, we can express the numerator, which is the joint probability to obtain the observed source counts (s_1, \dots, s_N), given the underlying source count rate cr_{SRC} as:

$$P(D|M) \equiv P(\{c_1, \dots, c_N\} | cr_{\text{SRC}}) = \prod_{i \leq N} P_{\text{pois}}(c_i, s_i + b_i). \quad (4)$$

Our 90 per cent confidence upper limit count rate (cr_{ul90}) based on the overlapped observations with different PSFs (or *Chandra* off-axis angles), exposures, and background levels can thus be obtained by solving:

$$0.9 = \frac{\int_0^{cr_{\text{ul90}}} P(\{c_1, \dots, c_N\} | cr_{\text{SRC}}) d cr_{\text{SRC}}}{\int_0^{\infty} P(\{c_1, \dots, c_N\} | cr_{\text{SRC}}) d cr_{\text{SRC}}}. \quad (5)$$

We also make the 90 per cent confidence upper flux limit maps of the different energy bands available as a FITS file on the VizieR Catalogue Service.

5.5 Low Likelihood Source Catalog

We generate a second source catalog with a lower maximum likelihood threshold (internal threshold of $ML = 5$; corresponding to $ML_{\text{empir}} \sim 9.5$ or a $\sim 4\sigma$ detection in the deep Subaru imaging region). We therefore have many more detected sources, but the fraction of spurious sources is also significantly higher. This catalog can be of interest if the scientific goal requires one to *exclude* potential X-ray emitting objects from a sample with a high completeness. Using this strategy, one accepts those objects that are excluded are *not* associated with an X-ray-emitting object. The catalog contains the same columns as real data source catalog with an internal threshold of $ML = 9.5$ (Sect. 5.2.1) and is also available from the VizieR Catalogue Service. We did not include any additional sources from the soft, medium, hard, 0.5–7 keV single band run, or 2–7 keV single band run that fulfill $ML \geq 5$. Our simulations show that including these additional sources with such a low maximum likelihood threshold in individual bands increases the spurious source fraction significantly. We therefore list only objects based on the joint source detection run of the three subbands that fulfill (internal) $ML_{0.5-7 \text{ keV}} \geq 5$.

This catalog contains 626 detected sources, of which 506 are located within the deep Subaru imaging region. Based on our simulated data, we conclude that 19 per cent of all catalog entries are false detections. Considering only the deep Subaru imaging area the spurious source fraction drops to 15 per cent. We significantly increase the completeness to 61 per cent for objects with at least four counts, ~ 85 per cent for objects with seven counts or more, and >95 per cent for sources with at least 12 counts. These numbers are based on considering all simulated input sources that have at least four counts in the total (added) observation and are located within the deep Subaru imaging region. Compared to the main source catalog, the total number of detected sources is increased by almost 40 per cent (174 objects). These additional sources contain a spurious source fraction of nearly 50 per cent. We therefore do not consider source detection runs with lower internal ML thresholds as scientifically meaningful. We emphasize again that due to the significant number of spurious sources in the catalog, it should *not* be used select X-ray sources or to increase the sample size of X-ray-selected objects.

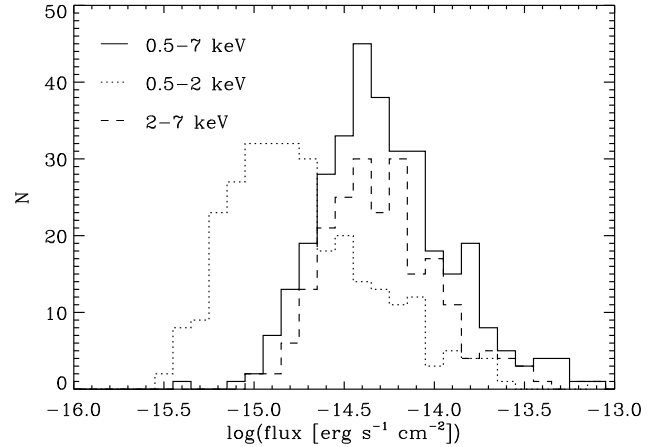


Figure 11. Flux histogram of the *Chandra*/AKARI NEP field sources selected with an internal threshold of $ML = 9.5$ and covered by the deep Subaru imaging data.

6 DISCUSSION

In this section we characterize the properties of the X-ray sources and the survey. We will focus only on the sources that are detected within the deep Subaru imaging region.

Figure 11 shows the observed source flux distribution. The histogram indicates the sensitivity limit of our survey in each energy band. The observed source flux distribution agrees well with the derived sensitivity maps in different energy bands. For example, our source detection falls short on detecting sources below $f_{0.5-7 \text{ keV}} \sim 10^{-14.4} \text{ erg s}^{-1} \text{ cm}^{-2}$ and $f_{0.5-2 \text{ keV}} \sim 10^{-15} \text{ erg s}^{-1} \text{ cm}^{-2}$ respectively. At the same fluxes the sensitivity maps in the different energy bands (see Fig. 10) reach the maximum survey area. Furthermore, Fig. 11 demonstrates that we detect sources down to, e.g., $f_{0.5-7 \text{ keV}} \sim 10^{-15} \text{ erg s}^{-1} \text{ cm}^{-2}$. This limit agrees also well with our derived sensitivity limit in this energy band.

6.1 $\log N - \log S$

To verify the accuracy of our sensitivity maps using an additional method, we create $\log N - \log S$ plots of different realizations of our simulated data sets in the *Chandra*/AKARI NEP field. We directly compare the $\log N - \log S$ relations of the simulated input table versus the recovered (`emldetect`) source list of this input table over two different simulations. The $\log N - \log S$ relation of the input source list can be calculated simply assuming a survey area twice as large as the geometrical area of the Subaru region (for the two simulations) at all fluxes.

The $\log N - \log S$ relation of the output list can be calculated by:

$$N(> S) = \sum_{S_i > S} \Omega_{\text{avail.}}(S_i)^{-1}, \quad (6)$$

where $\Omega_{\text{avail.}}(S_i)$ is the available survey area for the flux limit at or fainter than S_i over two simulations (see Fig. 10).

In order to verify our sensitivity map, we compare the $\log N - \log S$ curves of the detected sources from the simulated data set with that of the input source list. Figure 12 shows that the $\log N - \log S$ curve of the input catalog and

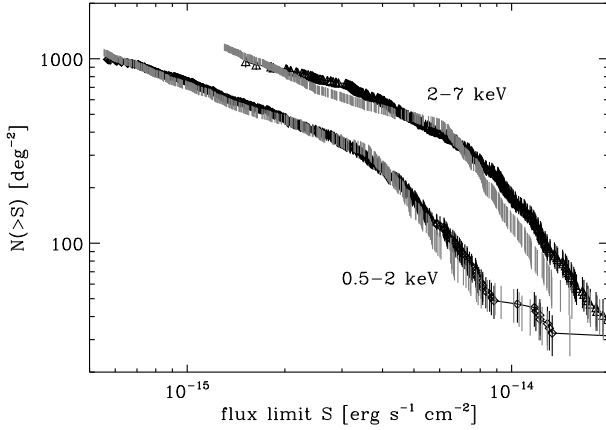


Figure 12. Cumulative number counts per area based on simulated data for the 0.5–2 keV and 2–7 keV band, respectively. The $\log N - \log S$ relation shown in black use the `emldetect` source list of simulated data and the available area considering the sensitivity maps in the corresponding energy band. In addition, we show in gray the $\log N - \log S$ relation based on the simulated input table and the total area of our survey. For both cases, we only consider the survey area that overlaps with the deep Subaru imaging data. The error bars represent 1σ uncertainties. The data presented here combine two simulated data sets.

detected sources from the simulated data sets agree within 1σ with that of the input catalog down to 5.5×10^{-16} and 1.3×10^{-15} $\text{erg s}^{-1} \text{cm}^{-2}$ for the 0.5–2 and 2–7 keV bands, respectively. Consequently, this consistency check demonstrates that our sensitivity map correctly represents the properties of the survey down to the flux limits shown above.

Figure 13 presents the $\log N - \log S$ plot of the real data in the 0.5–2 keV and 2–7 keV bands, respectively, using the final source catalog and the corresponding sensitivity maps. We compare the derived $\log N - \log S$ curves of our survey to other published works: the 1.8 Ms *Chandra* COSMOS survey (Elvis et al. 2009) and the ~ 4 Ms *Chandra* Deep Field South survey (CDF-S; Lehmer et al. 2012). To directly compare these surveys with our work, one has to account for different assumptions in computing the fluxes and different definitions of the energy bands. Consequently, we adjust the fluxes of the other surveys in such a way that they correspond to our Galactic-absorption corrected fluxes in the 0.5–2 keV and 2–7 keV bands based on $\Gamma = 1.4$. However, Lehmer et al. (2012) use a mix of individual photon indices for some sources, while for other sources they rely on the assumption that $\Gamma = 1.4$ as well. This limitation should be kept in mind, when comparing the CDF-S data with our survey.

The $\log N - \log S$ curves of the different surveys are similar (Fig. 13). Above $f_x \sim 5 \times 10^{-15}$ $\text{erg s}^{-1} \text{cm}^{-2}$, all surveys agree within their combined 1σ uncertainties. Below this flux, our derived cumulative number density is ~ 25 per cent higher than that of the CDF-S and ~ 12 per cent higher than that of the COSMOS survey. The difference in $\log N - \log S$ between COSMOS and CDF-S is similar to the one between our survey and COSMOS in the soft band. The deviations of our $\log N - \log S$ curves from those of COSMOS/CDF-S over the statistical error may thus be explained by field-to-field variation (cosmic variance). We also compute the $\log N - \log S$ relation for the whole *Chan-*

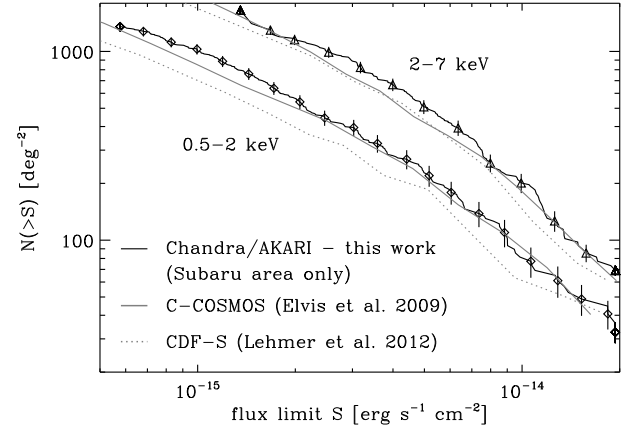


Figure 13. Cumulative number counts per area in the *Chandra/AKARI* NEP field (black solid line with data symbols; real data; deep Subaru imaging region only), the *Chandra* COSMOS field (gray solid line), and the *Chandra* Deep Field South survey (gray dotted line). For each survey, we show the $\log N - \log S$ relation for the 0.5–2 keV and 2–7 keV band. We do not show the error bars for the COSMOS and CDF-S survey, to preserve the clarity of the figure. However, the individual uncertainties are expected to be approximately the same as for the *Chandra/AKARI* NEP data.

dra/AKARI NEP deep survey and when excluding the regions around the two obvious galaxy clusters. All derived $\log N - \log S$ relations agree well within their 1σ statistical uncertainties.

6.2 N_{H} Column Densities from Hardness Ratios

Hardness ratios are the simplest tool to determine the spectral energy distribution in the X-ray regime. In addition, hardness ratios are commonly used to derive a first estimate of the absorbing column density (N_{H}) present in X-ray sources (e.g., Cappelluti et al. 2009; Krumpke et al. 2007, their Sect. 4.4). We follow this approach and simulate the expected range of hardness ratios corresponding to a range of values of intrinsic N_{H} for a grid of redshifts ($z = 0.0 - 3.0$; $\Delta z = 0.3$).

We use an X-ray spectral model (with $\Gamma = 1.8$) for Compton-thick toroidal reprocessors, specifically the MYTORUS model of Murphy & Yaqoob (2009), to account for Compton-reflected emission. This model assumes a “donut” morphology for the absorbing torus; it is homogeneous, of uniform density, and its half-opening angle is fixed to 60 deg. We assume full-covering absorption by an edge-on torus, in addition to the Galactic column. We also include a soft X-ray power-law whose photon index is tied to that of the primary hard X-ray power law. Such a component is frequently observed in Compton-thick absorbed Seyferts (e.g., Lira et al. 2002), and is commonly modeled as scattered power-law emission off diffuse, optically-thin gas. We assume an optical depth of $\tau = 0.02$ (e.g., Bianchi & Guainazzi 2007). However, the computed hardness ratios in the 0.5–2 and 2–7 keV band are degenerate with N_{H} . With increasing column density, the hardness ratio increases at first (as expected), but above a redshift-dependent value of N_{H} , the hardness ratio decreases. We break this degeneracy by considering only values of N_{H} on the increasing part of the hardness ratio

function (e.g., up to $6.3 \times 10^{22} \text{ cm}^{-2}$ at $z = 0$ or $1.6 \times 10^{24} \text{ cm}^{-2}$ at $z = 3$). This method is justified because we do not expect to be able to detect extremely-absorbed X-ray sources in our moderately deep overlapping observations.

An additional caveat of using the MYTORUS model is its built-in hard lower limit of $N_{\text{H}} = 10^{22} \text{ cm}^{-2}$. We therefore also compute the hardness ratios from a simple full-covering-absorption power law ($\Gamma = 1.8$). Both models agree very well within the transition region of a few $\times 10^{22} \text{ cm}^{-2}$. We thus use the hardness ratio predictions from our MYTORUS model for corresponding values of N_{H} above 10^{22} cm^{-2} , and hardness ratio from the simple absorbed power law for values of N_{H} below 10^{22} cm^{-2} .

Based on the u^* -band (CFHT/MegCam), B , V , R_c , i' , z' -band (Subaru/Suprime-Cam), J , and K_s -band (KPNO/Flamingos) images, Hanami et al. (2012) (hereafter H12), provide photometric redshifts of 56,000 z' -detected galaxies. For a few hundred IR sources, we also have spectroscopic redshifts from the team's Keck DEIMOS and Subaru FOCAS observations (Takagi et al. in preparation). Spectroscopic redshifts from the MMT Hectospec observations, emphasizing bright sources in the AKARI NEP Wide field (Shim et al. 2013), are also included. Additional data sets have been obtained after the analysis by Hanami et al. (2012). This includes CFHT WIRCAM YJK images (Oi et al. 2014) and Hectospec optical spectra (Shim et al. 2013), and further Keck DEIMOS, Subaru FMOS, and GTC OSIRIS observations. These data sets will be used in our future studies.

Using our final matching radius definition (Sect. 5.2), we cross-identify all X-ray detected sources with IR objects. In the rare cases (4 X-ray sources) that two IR objects fall within the X-ray matching radius, we consider the object that is brighter in the r -band to be the counterpart. This is justified because relatively brighter objects have a much lower surface density than fainter objects. Consequently, a brighter object has a higher probability to be the true counterpart compared to a fainter source. A more sophisticated approach (also considering the offset distance) will be taken in the future paper (Miyaji et al., in preparation). Roughly 60 per cent of all the 377 X-ray sources in the deep Subaru imaging region have AKARI-IR counterparts. Their redshift distribution is shown in Fig. 14.

We use the redshift information for our sources to derive column density N_{H} , based on the hardness ratio method described above. In order to not bias our study against absorbed AGN, we include in Fig. 15 all X-ray sources that have a signal-to-noise ratio of larger than 3 in the 2–7 keV band (i.e., $(f_{2-7}/\Delta f_{2-7}) > 3$). This approach allows us to also include objects that are very weak or not detected in the 0.5–2 keV band. The overall distribution of N_{H} does not significantly change when we moderately increase or decrease the signal-to-noise ratio.

Considering the uncertainties on N_{H} , 40 per cent of the X-ray sources are consistent with column densities $N_{\text{H}} \leq 10^{21} \text{ cm}^{-2}$. Half are consistent with absorption above a value of $N_{\text{H}} = 10^{22} \text{ cm}^{-2}$. The distribution in N_{H} for X-ray-absorbed objects peaks around a few $\times 10^{22} \text{ cm}^{-2}$. However, we expect that the location of the peak is subject to our limit in sensitivity in N_{H} , as the Chandra/AKARI survey is only moderately deep.

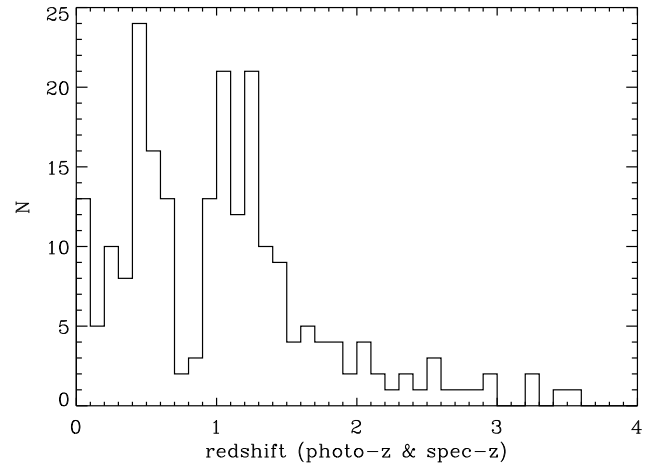


Figure 14. Redshift distribution of the IR counterparts of our X-ray sources. The redshifts are obtained mainly from photometric redshifts, but also from some spectroscopic observations.

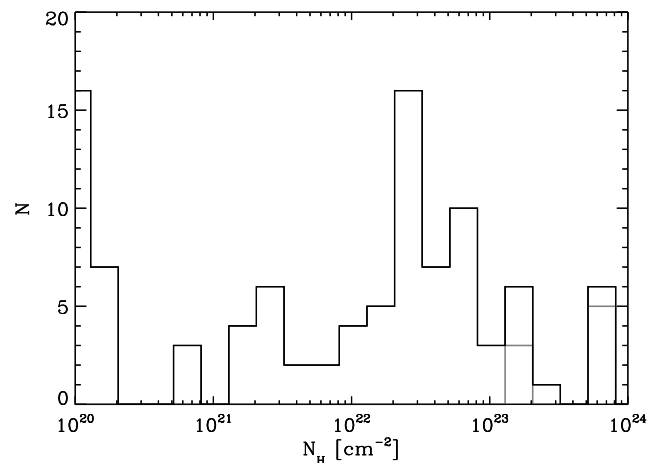


Figure 15. Histogram of the column density N_{H} for X-ray sources with IR counterparts and $(f_{2-7}/\Delta f_{2-7}) > 3$. N_{H} values are estimate from the X-ray hardness ratios and the redshift information of the IR counterparts. The objects denoted by the gray line have observed hardness ratios larger than the maximum predicted hardness ratio from our MYTORUS model. We assigned these object the value of N_{H} that corresponds to the maximum predicted hardness ratio of our MYTORUS model.

6.3 Cross-identification between X-ray and Optical Regime

We identify optical counterparts of our X-ray sources in the Subaru z' - and R_c -band. We consider again the brightest r -band object as the most likely counterpart, if more than one optical source falls within the X-ray matching radius.

Figure 16 shows the cumulative fraction of cross-identified X-ray sources normalized to the total number of X-ray sources (377 objects) as a function of z' - and R_c -band. For comparison purposes, we show the distribution of all z' -band objects (including X-ray undetected ones) as a function magnitude as well (normalized to the total number of z' -band objects). The fraction of cross-identified optical sources does not increase significantly beyond z' - and R_c -magnitudes of $m \sim 28$. It saturates at 77 per cent and 83 per

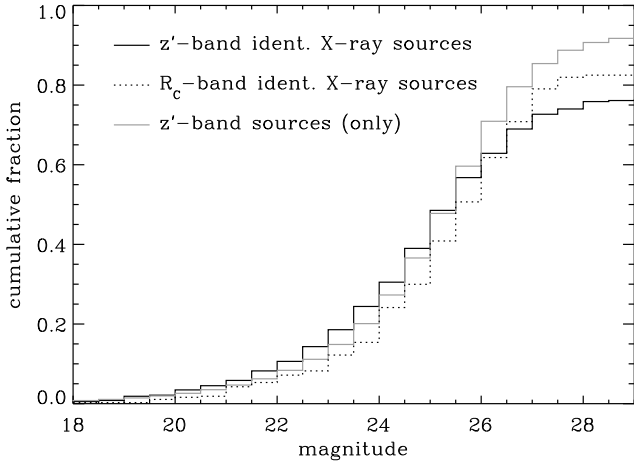


Figure 16. Cumulative fraction of optical counterparts vs. optical magnitude. The black solid and dotted line represent the cumulative fraction of cross-identified X-ray sources with z' -band and R_c -band objects, respectively. We use our final matching criterion given in Sect. 4.3.1. We only consider X-ray sources within the deep Subaru imaging region and an internal detection threshold of $ML = 9.5$. The gray solid line shows the fraction of Subaru z' -band sources with a magnitude equal or brighter the chosen value. For illustration purposes, we do not show data fainter than $m \sim 29$ where the z' -band sources (only) curve naturally approaches 1.

cent for objects in the z' - and R_c -band, respectively. Below $m \sim 26$, the z' -band is more efficient in identifying an optical counterpart of X-ray sources than the R_c -band. In the same magnitude range, the distribution of the cumulative fraction of X-ray sources with optical counterparts follows the general magnitude distribution of all z' -band Subaru sources.

6.4 Cross-identification between X-ray and Infrared Regimes

Having our X-ray source catalog, X-ray sensitivity, and X-ray upper limit maps, we perform a cross-matching with IR-selected AGN candidates by Hanami et al. (2012) (H12), who performed MIR SED fits based on the *AKARI* data. A major part of the analysis in H12 puts emphasis on objects that have been detected in at least three of the 7, 9, 11, 15, 18, and 24 μm bands in the *AKARI* NEP deep data out of their z' -band selected galaxy catalog with photometric redshifts of $z > 0.4$. This sample has been produced independently from the published *AKARI* NEP deep survey source catalog by Takagi et al. (2012).

In constructing their catalog, IR sources from regions around very bright objects are excluded to avoid any misidentification of the noise or tails of bright objects. Furthermore, sources with $m_{z'} < 18$ are excluded, as they might be saturated in the *AKARI* MIR data. Since most objects detected with *AKARI* have infrared luminosities of approximately $L_{\text{IR}} \gtrsim 10^{10} L_{\odot}$, H12 referred to this sample as their “Luminous Infrared Galaxies” (LIRGs), without imposing a hard cut in the IR luminosity of $> 10^{10} L_{\odot}$. Among those “LIRGs”, H12 searched for signatures of AGN. In our subsequent analysis, we use a slightly updated version of their

Table 2. Cross-identification of IR-selected AGN with X-ray sources

object class	IR-pure AGN $f_{\text{AGN}} = 1$	IR AGN/SB mix ^a $0.05 \leq f_{\text{AGN}} < 1$	IR-SBs $f_{\text{AGN}} = 0$
total LIRG [#]	42	213 (177)	149
in X-ray [#]	16	43 (43)	5
in X-ray [%]	38	20 (24)	3

^aThe numbers in parentheses are from excluding objects that cannot be detected even if the AGN are unabsorbed (see text).

$z > 0.4$ LIRG sample, involving newer photometric measurements. Hereafter, we refer to the updated sample of $z > 0.4$ “LIRGs” selected by these criteria simply as the LIRGs.

As described in H12, we fit the MIR data with Spectral Energy Distribution (SED) models that allow for a mixture of host galaxy and AGN emission. Each SED of the LIRGs is modeled by a series of starburst (SB) models from Siebenmorgen & Krügel (2007) and an AGN dusty torus component from the SWIRE library (Polletta et al. 2007). For each object, we have also computed the IR rest-frame luminosities of the AGN and SB contributions $L_{\text{IR,AGN}}$ and $L_{\text{IR,SB}}$ by integrating the fitted AGN and SB model SEDs from 8–1000 μm (rest-frame), respectively. We then define the “AGN fraction” (f_{AGN}) as the fraction of the total rest frame 8–1000 μm luminosity that comes from the dusty torus in the fit. Note that the short end of the used wavelength range contributes most to the constraints on the value of f_{AGN} since starburst galaxies without AGN activity have an emission dip around 3–8 μm (rest-frame). In other words, the $L_{\text{IR,AGN}}$ specifies only the contribution from the AGN and not the combined IR luminosity of the AGN and the host galaxy. Consequently, for objects with $f_{\text{AGN}} = 0$, $L_{\text{IR,AGN}} = 0$.

We use the AGN fraction to classify the LIRGs into three subgroups. The first contains objects in which the MIR SED is explained exclusively by AGN activity ($f_{\text{AGN}} = 1.0$; hereafter, IR-pure AGN). In the second group, we include all objects that require an additional starburst component in their SED, but their AGN contribution is still significant ($0.05 \leq f_{\text{AGN}} < 1.0$; hereafter, IR AGN/SB mix). For comparison, we also define a third group, which has $f_{\text{AGN}} = 0$, i.e., the observed IR SED of these objects is explained entirely by a starburst SED, and no IR AGN activity is detected.

Using our final matching radius definition (Sect. 5.2), we determine how many IR-selected sources in each subcategory are detected in the X-rays as well. The results are given in Table 2. When we offset the R.A. coordinate by +30 arcsec, no matching IR-selected object is found in any category. IR-selected AGN with $f_{\text{AGN}} = 1$ represent the group with largest fraction of X-ray detections. The X-ray detection rate decreases with decreasing AGN fraction. Since the vast majority of the X-ray sources are AGN, this independently confirms that the IR AGN selection method of H12 is able to select AGN successfully over a wide range of redshift and luminosity, based only on *AKARI* IR SED-fitting. In particular, the extremely small fraction of X-ray sources among $f_{\text{AGN}} = 0$ LIRGs shows that MIR SED-fitting utilizing the full *AKARI* MIR photometric bands is very ef-

ficient in separating non-AGN LIRGs from those that are (partially) powered by AGN.

A significant fraction of the IR-pure AGN and IR AGN/SB mix ($f_{\text{AGN}} \geq 0.05$) LIRGs still do not have X-ray counterparts. These may be due to the fact that: (a) AGN are highly absorbed in X-rays by (dusty or non-dusty) gas or (b) our X-ray sensitivity at their location is not sufficient to detect them. Our main scientific interest is the population of AGN that falls into category (a). A full assessment is beyond the scope of this paper, but will be discussed in paper II (Miyaji et al. in preparation).

Like the $L_{\text{IR,AGN}}$, the hard band (2–7 keV) luminosity is also a good proxy of the AGN luminosity in the X-ray regime. It is less affected by intrinsic absorption at the source than the 0.5–7 keV band, unless the absorbing column density is $N_{\text{H}} \gtrsim 10^{23.5} \text{ cm}^{-2}$. We compute the ratio of the 2–7 keV and IR AGN luminosities. For simplicity the K-correction of the X-ray flux to luminosity conversion assumes a pure power-law spectrum with a photon index of $\Gamma = 1.8$. Because the absorbed AGN in our sample have significantly different spectra, we use this K-correction (as well as count-rate to flux conversion assuming $\Gamma = 1.4$) for the purpose of the subsequent plots to obtain the “observed” X-ray luminosities L_{X} . On the other hand, the correct count rate to flux conversion and K-corrections based on a model spectrum of an AGN with $N_{\text{H}} = 10^{24} \text{ cm}^{-2}$ are used to draw corresponding model lines.

In Fig. 17, we show the ratio of observed 2–7 keV luminosity and $L_{\text{IR,AGN}}$ as a function of intrinsic column density estimated from the observed X-ray hardness ratios. All objects have a median X-ray to IR AGN luminosity ratio of $\langle L_{\text{X}}/L_{\text{IR}} \rangle = 0.09$ with a scatter within a factor of 2 when considering 68 per cent of all plotted objects. No significant difference in the distributions of $L_{\text{X}}/L_{\text{IR}}$ between IR-pure AGN ($f_{\text{AGN}} = 1$) and IR AGN/SB mix objects ($0.05 \leq f_{\text{AGN}} < 1$) is found.

An interesting quantity to derive from Fig. 17 is the median X-ray to IR AGN luminosity ratio for X-ray unabsorbed populations in IR-selected AGN with $f_{\text{AGN}} = 1$ (IR SED can be purely explained by AGN activity). Since most of the objects with $N_{\text{H}} < 10^{22} \text{ cm}^{-2}$ are consistent with unabsorbed column density, we apply this cut for our sample selection. Restricting ourselves to only $f_{\text{AGN}} = 1$ AGN minimizes the uncertainty of the IR luminosity. The median $L_{\text{X}}/L_{\text{IR}}$ for the sample of six objects that fulfill our criteria is 0.11.

The primary science driver for this survey is the identification of Compton-thick AGN candidates. A detailed quantitative study of the Compton-thick AGN population is the topic of a future paper (Miyaji et al., in preparation). Here, we make a quick-look analysis to select the Compton-thick AGN candidates based on the comparison between L_{X} and $L_{\text{IR,AGN}}$, assuming that the AGN IR-dusty torus component is unabsorbed and isotropic.

Figure 18 (left panel) shows the observed hard (2–7 keV) X-ray luminosity vs. AGN IR luminosity for the IR-pure AGN ($f_{\text{AGN}} = 1$). For IR-selected AGN that do not have a detected X-ray counterpart, we use the 90 per cent confidence upper flux limit to compute an upper limit on the 2–7 keV luminosity. Figure 18 also shows the constant line $L_{\text{X}}/L_{\text{IR}} = 0.11$, representing our X-ray unabsorbed AGN in the LIRG sample with $f_{\text{AGN}} = 1$. We find three IR-pure

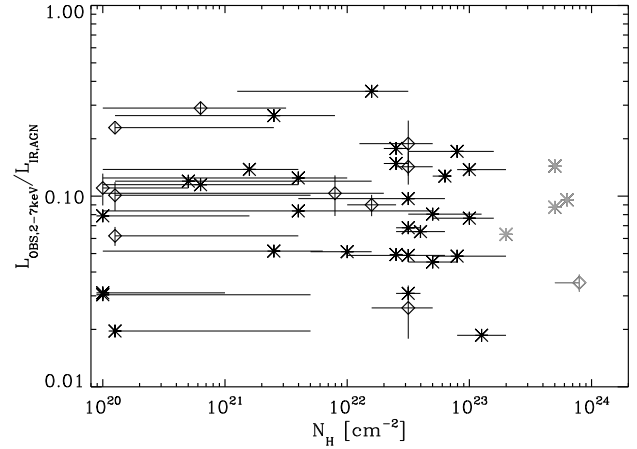


Figure 17. Ratio of AGN X-ray luminosity over AGN IR luminosity as a function of column density N_{H} . The plot includes IR-selected objects with AGN activity that have also been detected in the 2–7 keV band (internal threshold of $ML \sim 9.5$). Only X-ray sources with $(f_{2-7}/\Delta f_{2-7}) > 3$ are shown. Diamonds represent AGN with $f_{\text{AGN}} = 1$ (IR SED purely due to AGN activity), while stars indicate AGN with $0.05 \leq f_{\text{AGN}} < 1$. The horizontal lines show the 1σ uncertainties in N_{H} . For illustration purposes, we show the uncertainties on the ratio of X-ray to IR luminosity based on the error of the X-ray luminosity for the $f_{\text{AGN}} = 1$ AGN only. The objects plotted in gray have observed hardness ratios larger than the maximum predicted hardness ratio from our MYTORUS model. We assigned these objects the value of N_{H} that corresponds to the maximum predicted hardness ratio of our MYTORUS model.

AGN which are also detected in the X-rays and have spectroscopic data. These objects are classified as type I AGN (broad emission lines in the optical spectra). We show their location in the diagram. Type I AGN, as well as the X-ray detected objects for which we have only photometric redshifts (small squares), scatter around the derived median X-ray to IR-selected AGN luminosity ratio for unabsorbed AGN ($\langle L_{\text{X}}/L_{\text{IR}} \rangle = 0.11$).

We compute the ratio of $L_{\text{X}}/L_{\text{IR}}$ corresponding to $N_{\text{H}} = 10^{24} \text{ cm}^{-2}$ with our MYTORUS model as explained above. Because of the K-correction, this ratio depends on redshift, thus we calculate the ratio for $z = 0.5, 1.0$, and 1.5 . We consider a real Chandra ACIS response matrix and the model X-ray spectrum (MYTORUS) to calculate the decrease in the 2–7 keV count rate due to absorption. Then the decrease in the count rate is converted into a decrease in the observed X-ray luminosity to yield the lines with $N_{\text{H}} = 10^{24} \text{ cm}^{-2}$ in Fig. 18.

The upper limits of $L_{\text{X}}/L_{\text{IR}}$ for the X-ray non-detected IR-pure AGN have a median value of 0.017, which is close to the value expected from those with $N_{\text{H}} = 10^{24} \text{ cm}^{-2}$. The median redshift of the IR-selected AGN without X-ray detections is $\langle z \rangle \sim 1.0$. We also encode the redshift of the individual sources in the thickness of the arrows in Fig. 18 (increasing thickness = increasing redshift). The most promising Compton-thick candidates are the objects that have a ratio of $L_{\text{X}}/L_{\text{IR}}$ consistent with the presence of intrinsic column densities $N_{\text{H}} \geq 10^{24} \text{ cm}^{-2}$ at the object’s redshift. Consequently, we call those objects *strong Compton-thick AGN candidates* and those with upper limits of the $L_{\text{X}}/L_{\text{IR}}$ ratios indicating lower amount of absorptions *possible Compton-*

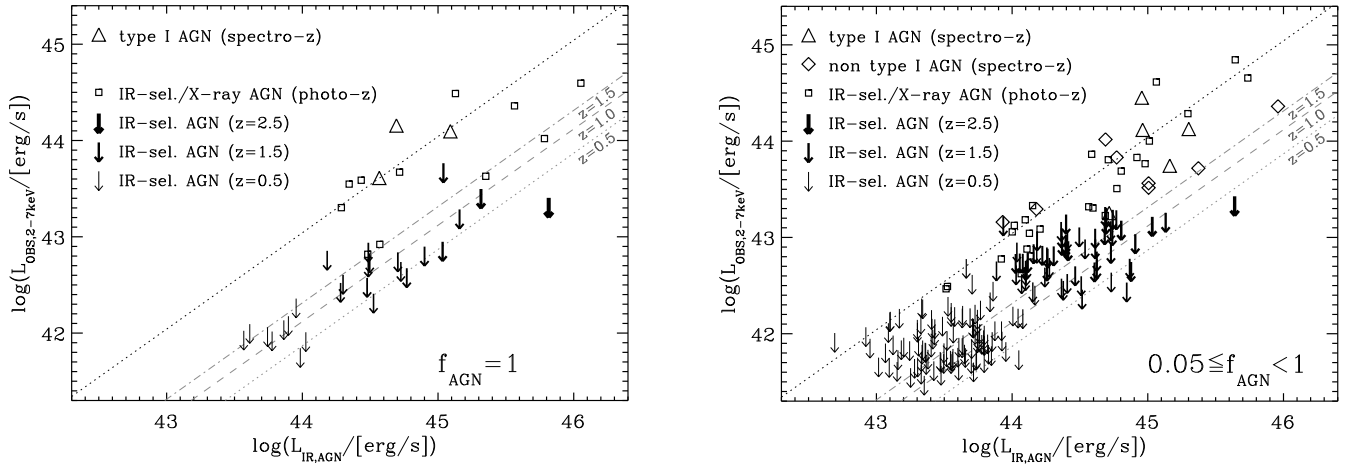


Figure 18. *Left:* Infrared (8–1000 μm) AGN rest-frame luminosity vs. hard (2–7 keV) observed X-ray luminosity. All objects shown have IR-SEDs purely explainable by AGN activity ($f_{\text{AGN}} = 1$). The different symbols represent: triangles – spectroscopically-confirmed type I AGN (broad emission lines), diamonds – objects with optical spectra that do not show broad emission lines, small squares – IR-selected AGN that are also detected in the 2–7 keV band with photometric redshifts (Hanami et al. 2012) only, downward arrows – IR-selected AGN that do not have a detection in the 2–7 keV band (internal threshold of $ML \sim 9.5$). For these objects, we use the 90 per cent confidence upper flux limit (see Sect. 5.4) in the 2–7 keV band. The thickness of the arrows encodes the redshift (continuous distribution) of the source. The black dotted line shows the correlation between the AGN IR luminosity and the X-ray luminosity ($\langle L_X/L_{\text{IR}} \rangle = 0.11$). The gray lines show for different redshifts the expected attenuation of the 2–7 keV X-ray luminosity caused by an intrinsic absorption of $N_{\text{H}} = 10^{24} \text{ cm}^{-2}$ using our MYTORUS model. *Right:* IR-selected objects where the AGN contribution to the total 8–1000 μm (IR) rest-frame luminosity is $0.05 \leq f_{\text{AGN}} < 1$.

thick AGN candidates, i.e., those that can have $N_{\text{H}} \geq 10^{24}$ if the L_X is lower than the observed upper limit. For those objects, deeper X-ray observations could determine whether they are strong Compton-thick AGN candidates or not.

Among the 26 IR-selected AGN with no X-ray detections (Fig. 18, left panel), we identify 10 (total sample: 42 IR-selected AGN) strong Compton-thick AGN and 16 possible Compton-thick AGN candidates. In addition, two IR-selected AGN that are detected in the X-ray fulfill the selection criterion for a strong Compton-thick AGN candidate. Therefore, roughly 30 per cent of all IR pure AGN ($f_{\text{AGN}} = 1$) are strong Compton-thick AGN candidates. This is in agreement with Brightman & Ueda (2012) who estimate that the Compton-thick AGN fraction at a redshift of $z \sim 1 - 4$ is about 40 per cent based on data from the CDF-S. Since the X-ray flux limit is known as a function of the position, we can count how many of them could not have been detected in 2–7 keV, even if it were not absorbed in X-rays, i.e., if $L_X/L_{\text{IR,AGN}} = 0.11$. None of the IR-pure AGN falls in that category.

We create the same figure for the IR AGN/SB mix objects ($0.05 \leq f_{\text{AGN}} < 1$; Fig. 18, right panel). This sample contains 170 IR-selected AGN with no X-ray detections. Their median $\langle L_X/L_{\text{IR,AGN}} \rangle = 0.031$. In comparison to Fig. 18 (left panel), these objects also have lower IR and X-ray luminosities.

Our sensitivity map shows that the X-ray limiting flux at the locations of 36 out of the 170 IR AGN/SB mix objects would also not be detected even if these AGN were unabsorbed. Consequently, excluding these 36 objects, the X-ray detection fraction among the IR AGN/SB mix is 24 per cent. These numbers are shown in Table 2 in parentheses. In these 170 non-X-ray-detected IR AGN/SB mix objects,

we find 15 strong Compton-thick AGN candidates and 119 possible Compton-thick AGN candidates.

7 SUMMARY

We present the data reduction, source catalog, sensitivity maps, 90 per cent confidence upper flux limit maps, and first analysis of the 300 ks *Chandra* survey in the *AKARI* North Ecliptic Pole deep field. The IR Camera onboard *AKARI* provides near-IR (NIR) to mid-IR (MIR) measurements with continuous wavelength coverage over 2–25 μm in 9 filters. This fills the 9–20 μm gap between the *Spitzer* IRAC+MIPS instruments, and allows efficient selection of AGN at $0.5 \lesssim z \lesssim 1.5$ in the IR. The *AKARI* NEP deep field is one of the deepest surveys ever achieved at $\sim 15 \mu\text{m}$, and is by far the widest among those with similar depths. Extensive multi-wavelength follow-up data from radio, sub-millimeter (*Herschel*), far-infrared, near-infrared, optical, and UV cover the *AKARI* NEP deep field.

Our *Chandra* observations further extend the wavelength coverage in this field to the X-rays. We use a dense ACIS-I pointing pattern to utilize the sharp *Chandra* PSF over the field to provide unambiguous identification. The total area covered by our *Chandra* mosaicked survey is $\sim 0.34 \text{ deg}^2$. Deep optical and near-infrared imaging has been obtained with Subaru/Suprime-Cam and covers the central $\sim 0.25 \text{ deg}^2$.

Our source detection algorithm uses a PSF-fitting code, based on the *XMM-Newton* Science Analysis System, which performs joint (simultaneous) Maximum Likelihood fits on each candidate source in sets of input images from several overlapping observations, and in multiple energy bands, accounting for the appropriate PSF model in each case. We

determine the optimal parameters for source detection by extensively testing our algorithm with simulated data sets. We implement several improvements compared to previously used versions of the code. As primary input, our algorithm uses three energy bands (0.5–2, 2–4, 4–7 keV) for each individual ACIS-I pointing. At the same level of spurious source fraction, we show that source detections (involving joint multi-PSF fittings) in subbands are preferred over a single broad band covering the same energy range. In addition, we demonstrate that the maximum likelihood threshold has to be calibrated by the spurious source fraction when using different numbers of detection bands and energy ranges.

The final source catalog yields in total 457 sources, of which 377 fall within the deep Subaru/Suprime-Cam imaging region. Based on the simulated data sets, we estimate a spurious detection rate of only ~ 1.7 per cent, and determine the optimal matching radius for each source to identify the corresponding counterpart in other wavelength ranges. We also list the properties of the sources in all bands. If sources are not detected in a certain band, we give the 90 per cent confidence upper flux limits, based on a Bayesian approach. We also produce sensitivity maps and 90 per cent confidence upper flux limit maps in each energy band. In addition, we generate a source catalog with a much lower maximum likelihood threshold. Since this catalog contains a much larger fraction of spurious detections, it is only of interest when one wants to *exclude* potential X-ray-emitting objects from a sample with a high completeness. Both catalogs and all maps are publicly available. We describe their format in detail.

Roughly 60 per cent of the X-ray sources have *AKARI* mid-IR counterparts. For those sources, we also have redshift information, and derive column density estimates based on the measured hardness ratios in the 0.5–2 and 2–7 keV bands. In the X-rays, we recover 38 per cent of the IR-selected AGN whose IR-SEDs originate only from AGN emission, and 20 per cent of the IR AGN in which a mixture of host galaxy starbursts and AGN is required for the MIR SED fits. The fraction decreases to 3 per cent if we consider those objects without any sign of AGN activity based on their MIR SED. We find a tight correlation between the 2–7 keV X-ray luminosity and the IR AGN luminosity. This confirms that the *AKARI* data in the NEP deep field are a powerful tool to identify successfully AGN over a wide range of redshift and luminosity.

Among the 42 IR-selected AGN (IR-SED exclusively explained by AGN activity), roughly 30 per cent are strong Compton-thick AGN candidates, where an absorbing column of $N_{\text{H}} > 10^{24} \text{ cm}^{-2}$ is suggested by $L_{\text{X}}/L_{\text{IR,AGN}}$, while another 16 objects are possible Compton-thick AGN, which are also not detected in X-rays, but the upper limits to $L_{\text{X}}/L_{\text{IR,AGN}}$ do not necessarily imply a Compton-thick column density. In the case of the IR-selected AGN that required an AGN and galaxy component to explain their IR-SED, only around 7 per cent (15 objects) are strong Compton-thick AGN candidates. However, 119 objects in this AGN subsample (~ 55 per cent) qualify as possible Compton-thick AGN. Deeper data are needed to verify them as strong Compton-thick AGN candidates. A detailed quantitative analysis of the Compton-thick AGN populations among the MIR selected AGN implied by our dataset is a topic of a future paper (Miyaji et al., in preparation).

The recently launched *NuSTAR* satellite (Harrison et al. 2010) is able to directly image X-rays above 10 keV. The results from *NuSTAR* are also expected to significantly expand our knowledge of the nature of Compton-thick AGN at cosmological distances. *NuSTAR* is limited in sensitivity. Thus, $E \lesssim 10$ keV X-ray and MIR diagnostics, as presented in this paper, will keep playing a complementary role in the census of Compton-thick accretion.

ACKNOWLEDGMENTS

We thank Georg Lamer for his simulations and making his results on the effect of the degree of freedom ML correction available to us. He also provided detailed comments on the appendix. We thank Richard Rothschild and Grant Tremblay for helpful discussions. In addition, we would like to thank the referee for valuable comments that improved the paper.

The research leading to these results has received funding from the European Community’s Seventh Framework Programme (/FP7/2007-2013/) under grant agreement number 229517. Support for this work was provided by the National Aeronautics and Space Administration through Chandra Award Number GO1-12178X issued by the Chandra X-ray Observatory Center, which is operated by the Smithsonian Astrophysical Observatory for and on behalf of the National Aeronautics Space Administration under contract NAS8-03060. Furthermore, we acknowledge the support by CONACyT Grant Científica Básica #179662, UNAM-DGAPA Grants PAPIIT IN104113. HH and TI thank the Grant-in-Aids for Scientific Research (24650145) and (26400216) from Japan Society for the Promotion of Science (JSPS) respectively, which partially supported this research.

This research has made use of data obtained from the Chandra Mission and software provided by the Chandra X-ray Center (CXC) in the application packages CIAO, ChIPS, and Sherpa. This research is based on observations with *AKARI*, a JAXA project with the participation of ESA. This research has made use of the VizieR catalogue access tool, CDS, Strasbourg, France.

REFERENCES

- Bianchi S., Guainazzi M., 2007, AIPC, 924, 822
- Brand K., Dey A., Weedman D., et al., 2006, ApJ, 644, 143
- Brightman M., Ueda Y. 2012, MNRAS, 423, 702
- Cappelluti N., Brusa M., Hasinger G., et al., 2009, A&A, 497, 635
- Cash W., 1979, ApJ, 228, 939
- Damiani F. et al., 1997, ApJ, 483, 350
- Donely J.L. et al., 2012, ApJ, 748, 142
- Elvis M. et al., 2009, ApJS, 184, 158
- Freeman P.E. et al., 2002, ApJS, 138, 185
- Fruscione A. et al., 2006, SPIE, 6270, 60
- Gabriel C. et al., 2004, ASPC, 314, 759
- Gilli R., Comastri A., Hasinger G., 2007, A&A, 463, 79
- Hanami H., Ishigaki T., Fujishiro N., et al., 2012, PASJ, 64, 70

- Harrison F.A. et al., 2010, SPIE, 7732, 27
 Ishihara D. et al., 2010, A&A, 514, 1
 Kalberla P.M.W. et al., 2005, A&A, 440, 775
 Kim M. et al., 2007, ApJS, 169, 401
 Kraft R.P., Burrows D.N., Nousek J.A., 1991, ApJ, 374, 344
 Krumpke M., Lamer G., Schwobe A.D., et al., 2007, A&A, 466, 41
 Lacy M. et al., 2007, AJ, 133, 186
 Larson D. et al., 2011, ApJS, 192, 16
 Lehmer B.D., Xue Y.Q., Brandt W.N., et al., 2012, ApJ, 752, 46
 Lira P., Ward M., Zezas A., et al., 2002, MNRAS, 330, 259L
 Martínez-Sansigre A. et al., 2005, Natur, 436, 666
 Matsuhara H., Shibai H., Onaka T., Usui, F., 2005, AdSpR, 36, 1091
 Matsuhara H., 2006, PASJ, 58, 673
 Murakami H., Baba H., Barthel P. et al., 2007, PASJ, 59, 369
 Murphy K.D., Yaqoob T., 2009, MNRAS, 397, 1549
 Oi N., et al., 2014, A&A, 566, 60
 Polletta M., Tajer M., Maraschi L., et al. 2007, ApJ, 663, 81
 Puccetti S., et al., 2009, ApJS, 185, 586
 Rumbaugh N., et al., 2012, ApJ, 746, 155
 Shim H., Im M., Ko J., et al. 2013, ApJS, 207, 37
 Siebenmorgen R., Krügel E., 2007, A&A, 461, 445
 Soltan A., 1982, MNRAS, 200, 115
 Takagi T. et al., 2012, A&A, 537, 24
 Teplitz H.I., Charmandaris V., Chary R., Colbert J.W., Armus L., Weedman D., 2005, ApJ, 634, 128
 Toba, Y. et al., 2014, ApJ, 788, 45
 Ueda Y., Akiyama, M., Ohta, K., Miyaji, T., 2003, ApJ, 598, 886
 Wada T. et al., 2008, PASJ, 60, 517
 Watson M. G. et al., 2009, A&A, 493, 339
 Xue Y. et al., 2011, ApJS, 195, 10

APPENDIX A: COMPARING A JOINT DETECTION IN 3 SUBBANDS WITH A SINGLE-BAND RUN

A1 Details on the Origin of Divergent ML Values

In Section 4.2.4, we point out that the value of the detection likelihood ML cannot be used blindly for different numbers of energy (sub)bands. Instead it should be calibrated by aiming for the same spurious source fraction using simulated data sets. In the following, we use such calibrated source detection runs with different numbers of subbands but covering the same energy range. The issue arises because likelihoods from different bands are combined and then normalized to two degrees of freedom (see Eq. 1 and Sect. 4.2.3). This normalization of the final ML is always applied, even in the case of a single broad band detection run.

Figure A1 illustrates the problem for two source detection runs that cover an identical energy range, but where one uses a joint 3-subband detection while the other uses a single energy band detection. Figure A1 shows that for bright sources, the ML values of both methods follow a 1:1

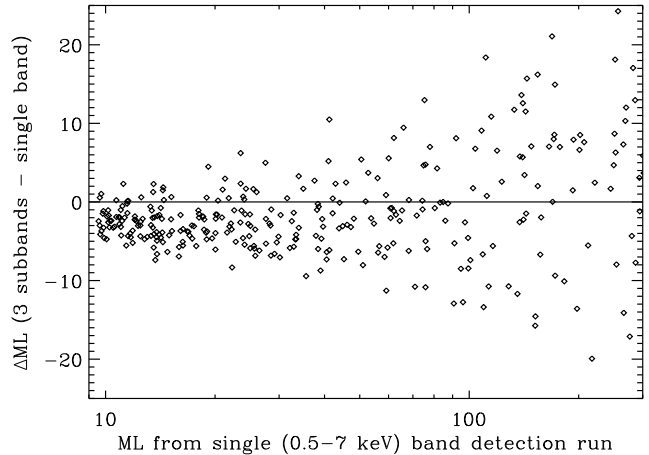


Figure A1. Comparison of the maximum likelihood values for the same simulated input sources (true sources) based on a 0.5–7 keV source detection using a single band and a joint detection run in 3 subbands (0.5–2, 2–4, 4–7 keV). The y-axis shows the difference between the likelihood values from 3-subband vs. a single broad energy band.

correlation. Only for faint sources do both ML values deviate significantly. The joint 3-subband detection run returns lower ML values on average than the single-band detection for the same simulated input source.

Each subband contributes one additional degree of freedom to the PSF fits (the source flux in that band). The normalization to two degrees of freedom thus results in a larger downward correction of the likelihoods in the case of our 3 band detection run as compared to the single-band run. We suspect, however, that the likelihood normalization introduces an over-correction to the likelihoods of faint sources, since subbands that contain no counts at all in the source extraction region do not justify an additional degree of freedom. The algorithm reaches its limitation if i) an object is too faint to contain a count in a certain subband or even in several subbands or ii) the number of background counts in a subband is too low (or even zero). Simulating different levels of background and source counts, we verify that the applied procedure works correctly in the case of large numbers of background counts in single bands. For small count numbers, the likelihood values have to be calibrated by simulations. One should thus not compare the number of source detections from different source detection runs in different surveys, or even within the same survey, only based on the ML threshold value.

The problem is not as prominent in *XMM-Newton* data, as these data have a much higher background and the instrumental PSF is much larger. Each subband thus has a higher chance to contain, within an area of 80 per cent of the PSF, enough background counts to justify the assumption. In our case of having very sharp *Chandra* PSFs, with low background, and multiple overlapping pointing for a single source in which the individual pointings have rather low exposure time (therefore low counts), the issue is recognizable for faint sources. However, as mentioned before, we can correct for this by normalizing different source detection runs to the same spurious source fraction.

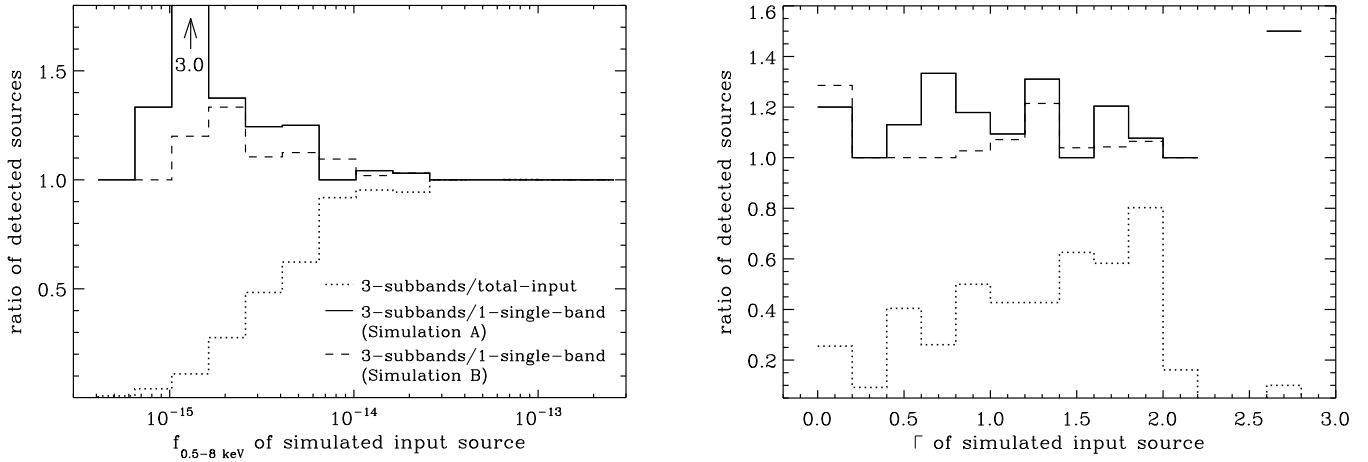


Figure A2. *Left:* Ratio of detected sources in 3 subbands over one single-band source detection (solid and dashed line) as the function of 0.5–8 keV simulated input flux. The solid and dashed lines represent different simulated data sets. Due to illustration purposes, we cut the y-axis at 1.8, although in the case of Simulation A, the y-value for the bin around $1.5 \times 10^{-15} \text{ erg s}^{-1} \text{ cm}^{-2}$ is 3.0. The dotted line shows the detection ratio of sources from the 3-subband run over the total number of simulated input sources that have at least four counts when adding all our pointings. The dotted line represents the average from Simulation A + B. *Right:* The same ratios are plotted, but this time as a function of the effective photon index Γ of the simulated input source. At $\Gamma \sim 2.7$, there was no detected source in the single-band source detection run and one detected source in the 3-subband run. We therefore artificially rescale this value to 1.5 solely for illustration purposes.

A2 Details on the Difference of Detected Sources

The 3-subband source detection run detects 5–10% more sources than the single-band run. To understand the difference, we study the properties of the detected X-ray sources for both methods. We are able to do so, as we can rely on our extensive simulated data sets in which we have access to the input flux, input counts, and effective photon index Γ for each source. Instead of N_{H} and intrinsic Γ , we use for our simulations an effective Γ which represents the general shape of the X-ray spectrum of the source.

Figure A2 (left) shows that the additional simulated input sources detected by the 3-subband run are found at fainter X-ray fluxes compared to the single-band run. The 3-subband run is more sensitive to detect weak, but true simulated input sources. This happens at fluxes where the overall fraction of detected sources, compared to all input sources with at least four counts, drops significantly. Based on our spurious source fraction criterion ($\sim 2\%$) and first simulations, we know that a source has to have approximately four counts to be contained in the final source catalog even if it is observed on-axis.

Interestingly, these additional sources are found across all values of effective Γ (Fig. A2, right). In other words, it is not the case that the additional detected sources are extremely soft or hard. We verify this finding by comparing the 2–4/0.5–2 keV count rate hardness ratio to the 4–7/2–4 keV hardness ratio for the detected sources. The sources from a single broad energy run occupy the same area as the additional (true) sources that are only detected in the joint 3-subband detection run.

Figure A2 (right) also shows that the source detection algorithm recovers most simulated input sources at effective $\Gamma \sim 1.5 - 2.0$. This range corresponds to unabsorbed or only mildly absorbed X-ray sources. For these studies, we only consider simulated input sources that have at least four

counts in the energy range 0.5–7 keV. The overall efficiency of detecting strongly absorbed (effective $\Gamma \sim 0.0 - 0.5$) simulated input sources is significantly lower than for unabsorbed sources.

To summarize, the joint (simultaneous) detection in subbands is preferred over a detection in a single band covering the same energy range, as it detects more faint sources. A likely explanation is that a faint source might be detectable with a higher *ML*-value (higher contrast between source counts and background) in a single subband, while a single broad energy band contains relatively more background resulting in a decrease in contrast.